



โครงการการเรียนการสอนเพื่อเสริมประสบการณ์

เรขาคณิตและการกระจายตัวของรอยแตกจุลภาคและเคอโรเจน
ในหินดินดาน จากแอ่งพิษณุโลก

โดย

นายพิชญ โหตรภวานนท์

เลขประจำตัวนิสิต 5832728723

โครงการนี้เป็นส่วนหนึ่งของการศึกษาระดับปริญญาตรี
ภาควิชาธรณีวิทยา คณะวิทยาศาสตร์ จุฬาลงกรณ์มหาวิทยาลัย

ปีการศึกษา 2561

บทคัดย่อและแฟ้มข้อมูลฉบับเต็มของโครงการทางวิชาการที่ให้บริการในคลังปัญญาจุฬาฯ (CUIR)

เป็นแฟ้มข้อมูลของนิสิตเจ้าของโครงการทางวิชาการที่ส่งผ่านทางคณะที่สังกัด

The abstract and full text of senior projects in Chulalongkorn University Intellectual Repository (CUIR)

are the senior project authors' files submitted through the faculty.

เรขาคณิตและการกระจายตัวของรอยแตกจุลภาคและเคอโรเจน
ในหินดินดาน จากแอ่งพิชญ์โลก

นายพิชญ์ โหตรภวานนท์

โครงการนี้เป็นส่วนหนึ่งของการศึกษาตามหลักสูตรวิทยาศาสตรบัณฑิต
ภาควิชาธรณีวิทยา คณะวิทยาศาสตร์ จุฬาลงกรณ์มหาวิทยาลัย
ปีการศึกษา 2561

Geometry and distribution of microcracks and kerogen
in shales from the Phitsanulok Basin

Mr. Pitchaya Hotarapavanon

A Project Submitted in Partial Fulfillment of the Requirements
for the Degree of Bachelor of Science Program in Geology
Department of Geology, Faculty of Science, Chulalongkorn University
Academic Year 2018

หัวข้อโครงการ

เรขาคณิตและการกระจายตัวของรอยแตกจุลภาคและ
เคอโรเจนในหินดินดาน จากแอ่งพิษณุโลก

โดย

นายพิษณุ โหตรภวานนท์

สาขาวิชา

ธรณีวิทยา

อาจารย์ที่ปรึกษาโครงการหลัก

ผู้ช่วยศาสตราจารย์ ดร.วรัญทร คณิตปัญญาเจริญ

วันที่ส่ง..... 13 พ.ค. 2562

วันที่อนุมัติ..... 13 พ.ค. 2562

.....
Waranteru

อาจารย์ที่ปรึกษาโครงการหลัก
(ผู้ช่วยศาสตราจารย์ ดร.วรัญทร คณิตปัญญาเจริญ)

Project Title Geometry and distribution of microcracks and kerogen in shales
 from the Phitsanulok Basin

By Mr. Pitchaya Hotarapavanon

Field of Study Geology

Project Advisor Assistant Professor Waruntorn Kanitpanyacharoen, Ph.D.

Submitted date..... 13 May 2019.....
Approval date..... 13 May 2019.....

Waruntorn.....

Project Advisor

(Assistant Professor Waruntorn Kanitpanyacharoen, Ph.D.)

พิชญ โหตรภวานนท์ : เรขาคณิตและการกระจายตัวของรอยแตกจุลภาคและเคอโรเจนในหินดินดาน จาก
แอ่งพิชญโลก (GEOMETRY AND DISTRIBUTION OF MICROCRACKS AND KEROGEN IN SHALES
FROM THE PHITSANULOK BASIN) อ.ที่ปรึกษาโครงการหลัก : ผู้ช่วยศาสตราจารย์ ดร.วรัญทร คณิต
ปัญญาเจริญ, 44 หน้า.

หินดินดานเป็นหินตะกอนที่ประกอบด้วยเม็ดตะกอนขนาดเล็ก สารประกอบอินทรีย์หรือเคอโรเจน รูพรุน
ขนาดเล็ก และรอยแตกจุลภาค แต่อย่างไรก็ตามโครงสร้างขนาดเล็กภายในหินดินดานทำให้ยากต่อการศึกษาด้วย
วิธีการทั่ว ซึ่งรอยแตกจุลภาคที่ไต่กล้ำมานี้สามารถเกิดขึ้นจากการปลดปล่อยสารไฮโดรคาร์บอนจากสารประกอบ
อินทรีย์ในหินเมื่อได้รับความร้อนเป็นเวลานาน รอยแตกจุลภาคเหล่านี้ยังส่งผลถึงค่าความซึมผ่านของหินให้เพิ่ม
มากขึ้น ทั้งนี้การศึกษาและเข้าใจถึงลักษณะจำเพาะในหินดินดานยังมีส่วนในการพัฒนาทางด้านปิโตรเลียมและ
วิทยาศาสตร์สิ่งแวดล้อมอีกด้วย ตัวอย่าง หินดินดานจำนวน 3 ตัวอย่าง จากหลุมเจาะเดียวกันในชุดหินขุมแสงจาก
แอ่งพิชญโลก ถูกนำมาใช้ในการศึกษาคั้งนี้ โดยใช้วิธีการถ่ายภาพตัดขวางด้วยรังสีเอ็กซ์จากแหล่งกำเนิดแสงซินโค
ตรอน ด้วยวิธีการนี้ทำให้ได้ภาพที่มีความละเอียดเพียงพอต่อการศึกษาโครงสร้างจุลภาคเช่น รูพรุน รอยแตก
จุลภาค และเคอโรเจน ผลจากการศึกษาในครั้งนีชี้ให้เห็นว่า ในตัวอย่างหินดินดานประกอบด้วยรูพรุนหลากหลาย
ชนิด เช่น รูพรุนระหว่างเม็ดตะกอน รูพรุนภายในเม็ดตะกอน รูพรุนในสารอินทรีย์ และรูพรุนจากรอยแตกจุลภาค
โดยพบว่ารูพรุนในสารอินทรีย์มักพบร่วมกับรอยแตกจุลภาคที่พบตามขอบของเคอโรเจนและรอยแตกจุลภาคที่วาง
ตัวตั้งฉากกับมวลเคอโรเจน สำหรับค่าความพรุนที่วัดได้จากการสร้างแบบจำลองสามมิติ พบว่าทั้งสามตัวอย่างจาก
แอ่งพิชญโลก มีค่าความพรุนตั้งแต่ 1.12 ถึง 1.98 เปอเซ็นต์ ซึ่งส่วนมากเป็นรูพรุนที่มาจากรอยแตกจุลภาค
สำหรับรูพรุนประเภทอื่นที่พบมีปริมาณน้อยมากเมื่อเทียบกับปริมาณรูพรุนทั้งหมด ส่วนเคอโรเจนมีค่าอยู่ในช่วง
1.93 ถึง 12.97 เปอเซ็นต์โดยปริมาตร รูพรุนส่วนมากและเคอโรเจนมีรูปร่างคล้ายรอยแตกและเป็นแผ่น โดยมี
อัตราส่วนความกว้างต่อความยาวเป็น 0.27 และ 0.34 ตามลำดับ โดยทั้งรอยแตกจุลภาคและเคอโรเจนจะวางตัว
ค่อนข้างขนานซึ่งกันและกัน ทำมุมไม่เกิน 7 องศา และขนานกับแนวระนาบชั้นหิน นอกจากนี้แล้วรอยแตกยังส่ง
ผลให้ค่าความซึมผ่านของของไหลในหินดินดานมีค่าสูงขึ้นด้วย

ภาควิชา _____ ธรณีวิทยา _____ ลายมือชื่อนิสิต _____
สาขาวิชา _____ ธรณีวิทยา _____ ลายมือชื่อ อ.ที่ปรึกษาหลัก _____
ปีการศึกษา _____ 2561 _____ ลายมือชื่อ อ.ที่ปรึกษาร่วม _____

5832728723 : MAJOR GEOLOGY


KEYWORD : MICROSTRUCTURE / MICROCRACKS / KEROGEN / GEOMETRY / DISTRIBUTION / SHALE

PITCHAYA HOTARAPAVANON : GEOMETRY AND DISTRIBUTION OF MICROCRACKS AND

KEROGEN IN SHALES FROM THE PHITSANULOK BASIN : ASSISTANT PROFESSOR

WARUNTORN KANITPANYACHAROEN, Ph.D., 44 pp.

Shale is a fine-grained sedimentary rock, comprising of clay-sized particles, organic matter or kerogen, micropores, and microcracks. An assessment of quality in shale is difficult to observe under general optical instruments due to the micro-scale features. Microcrack in shale is potentially related to fluid overpressure by the expulsion of hydrocarbon from organic matter during maturation. The microcrack causes a significant increase in permeability. Therefore, a good understanding of shale characteristics is needed to develop petroleum industry and waste storage technology. Three shale samples were collected from the same borehole in Chumsaeng formation, the Phitsanulok Basin. X-ray computed tomography with synchrotron light source produced high-resolution 3D images for investigation of micro-scale materials such as pores, microcracks, and kerogen in shale samples. Results from this research suggest that various pore types including interparticle pores, intraparticle pores, organic-matter pores, and fracture pores (microcracks) were found in shale samples. Organic-matter pores often coexist with perpendicular cracks and kerogen edge cracks. Porosities in shale samples are ranging from 1.12-1.98% mainly calculated from microcracks. Other minor pore types such as interparticle pore and intraparticle pore were found and accounted for very small volume. Kerogen values have a wide range of 1.93-12.97% by volume. Major pores in samples have crack-like geometry (average aspect ratio = 0.27), while kerogen has patch-like geometry (average aspect ratio = 0.34). Microcracks and kerogen have obvious orientation parallel to each other and bedding plane with inclination less than 7%. Moreover, these cracks significantly influence fluid transport properties of shale.

Department :Geology..... Student's Signature 

Field of Study :Geology..... Advisor's Signature 

Academic Year :2018..... Co-advisor's Signature _____

ACKNOWLEDGMENTS

It is a great pleasure to express the unwritable moment of gratitude to everyone who has inspired and supported me. The entire year of senior has flown by, faster than expected. I have learned and gained many experiences and knowledge. It has ensured me that hard works do make a man disciplined and strong. All of these achievements cannot be real without our supervisor, Asst. Prof. Dr. Waruntorn Kanitpanyacharoen. I would like to acknowledge her for helpful suggestions and open-minded understanding of all problems. I would also like to thank all lecturers for fundamental knowledge. The project has been done on a good basis of geology. Another most important thing is powerful encouragement from my family and friends. I believe deeply that the foundation of accomplishment is started from desires and the encouraged mind.

Mr. Pitchaya Hotarapavanon

Author

List of Contents

Abstract in Thai	V
Abstract in English	VI
Acknowledgments	VII
List of Contents	VIII
List of Figures	X
List of Tables	XIII
Chapter I Introduction	
1.1 Background	1
1.2 Literature reviews	1
1.3 Objective	4
Chapter II Geology of study area	
2.1 Geological setting	5
2.2 Stratigraphy and depositional environment	10
2.3 Petroleum system	14
Chapter III Methodology	
3.1 Sample preparation	19
3.2 Synchrotron X-ray micro-computed tomography imaging technique	19
3.3 Data analysis	21
Chapter IV Results	
4.1 2D observations	25
4.2 Volume fractions and size distributions	28
4.3 3D geometry and orientation	32

Chapter V Discussions and conclusion

5.1 Discussions 37

5.2 Conclusion 40

References 41

List of Figures

Figure 1.1	Microfracture development before and after a stage of pyrolysis	2
Figure 1.2	The change in Green River shale during heating	3
Figure 1.3	The geometry and 3D distribution from different synchrotron facilities	4
Figure 2.1	Location of the Phitsanulok Basin and other Cenozoic basins	5
Figure 2.2	The Phitsanulok Basin, the Uttaradit and Mae Ping fault zones	6
Figure 2.3	Regional tectonic elements and major strike-slip fault	7
Figure 2.4	W-E cross-section of the Phitsanulok Basin	8
Figure 2.5	The structural development of the Phitsanulok Basin	9
Figure 2.6	Stratigraphy and depositional environment of the Phitsanulok Basin	10
Figure 2.7	Schematic depositional environment of Sarabop Formation, Nong Bua Formation, and Khom Formation	11
Figure 2.8	Schematic depositional system of Lan Krabu Formation and Chum Saeng Formation	12
Figure 2.9	Paleogeography of Tertiary sedimentary units of the Phitsanulok basin	13
Figure 2.10	1D petroleum system modeling from well SBP-A01	15
Figure 2.11	Schematic stratigraphy of sedimentary units across the Phitsanulok Basin	16
Figure 2.12	The maturity of Chum Saeng Formation under Sukhothai depression	18
Figure 3.1	Schematic diagram of Synchrotron X-ray micro-computed tomography (Syn-MCT) equipment	19

Figure 3.2	Beer-Lambert's law, the relationship between intensity of light and the material's absorption coefficient	20
Figure 3.3	Data reconstruction workflow of Barnett shale sample	21
Figure 3.4	Workflow of data analysis processing	22
Figure 3.5	Noise observation in a raw image before and after 3D median filter	23
Figure 3.6	Component classification on greyscale of pyrite, kerogen, pore and microcrack	23
Figure 3.7	3D segmentation of microcracks in sample PHS02-3 before and after small spots removal	24
Figure 4.1	2D reconstruction images from all VOIs	25
Figure 4.2	2D image of PHS01-4 shows fracture pore, kerogen patch, and pyrite framboids	26
Figure 4.3	2D images of PHS01-2 and PHS01-3 show fossils trace with pores in fossil bodies	27
Figure 4.4	Pores between grains in PHS02-4 and PHS03-3 and pore at the edge of rigid grain in PHS03-3	27
Figure 4.5	Organic-matter pores in PHS01-1 comparing to organic-matter pores in PHS02-3	27
Figure 4.6	Perpendicular cracks on the kerogen patch	28
Figure 4.7	3D segmentation of pore, kerogen, and pyrite illustrated from PHS01-3, PHS02-3, and PHS03-4	29
Figure 4.8	Scatter plot between porosity and kerogen	31

Figure 4.9	Histograms and cumulative percentage of microcracks and kerogen	32
Figure 4.10	Width-length plot and aspect ratio histogram of microcracks and kerogen	33
Figure 4.11	Views on XY plane of 3D segmentation show the orientation of microcrack and kerogen	35
Figure 4.12	Rose diagrams of microcracks and kerogen orientation	36

List of Tables

Table 2.1	Basic properties of Sirikit oil	15
Table 3.1	Volume of cracks comparison after processing “Remove small spots” in PHS02-3	24
Table 4.1	Conclusion of features present in sample PHS01, PHS02, and PHS03	28
Table 4.2	Quantity of pore, kerogen, and pyrite of PHS01, PHS02, and PHS03	30
Table 5.1	Comparison of porosity, kerogen, and permeability in shale from other studies	38
Table 5.2	Comparison of permeabilities in X, Y, and Z axes	39

CHAPTER I

INTRODUCTION

1.1 Background

World population has significantly increased as well as the demand for fossil fuel and advanced environmental technology. Among natural resources, shale plays an important role in energy exploration and production as it contains a large number of organic materials. Shale can serve as a reservoir and source rock both of conventional and unconventional hydrocarbon reservoirs. Shale also has an importance in trapping due to its impermeable property. By this property causes shale to become a cap rock for a reservoir in a petroleum system. Certainly, this trapping ability in shale can be analog to trapping toxic waste.

Shale is a fine-grained sedimentary rock deposited in quiet environments such as lacustrine, fluvial, alluvial, and delta. shale comprises clay-sized particles, and organic materials and present microstructures such as micropore, and microcrack. By the time that the rocks are buried into the deeper subsurface, temperature and pressure are increased. One of the organic materials known as kerogen can be decomposed and generate a hydrocarbon under a high-temperature condition. Once the hydrocarbon is generated, the fluid creates overpressure that can cause deformation structure of rock like microcrack. The microcrack affects to porosity and permeability of the rock. The challenge in this study is difficulty in observation and measurement micro-scale features of shale. Therefore, X-ray Tomography microscopy with Synchrotron light source is required to characterize three-dimensional microstructures, geometry, and distribution of different materials.

A study of shale properties by the method we used is not currently widespread in Thailand. So, the samples we collected are from a petroleum-related field from the Phitsanulok Basin which is the largest onshore crude oil-recovered field in Thailand. The rocks that contain high kerogen in this basin are from the Chum Saeng formation, the Oligocene lacustrine shale. Accordingly, we chose the Phitsanulok Basin as a study area.

1.2 Literature reviews

Organic-rich shales from Kimmeridge (TOC=5.96 and 10.09%wt) and the organic-poor shale from Woodford (TOC=2.26%wt) have been observed by scanning electron microscopy and effective porosity measurements before and after heating with the absence of oxygen condition

(pyrolysis). This experiment reveals that microfractures initiate in the patch of kerogen when fluids are produced and fluid pressure increases. And then the microfractures propagate along the direction of the layer of kerogen (Allan et al., 2014). One series of experiment was performed with a small amount of confining pressure and show some perpendicular fracture networks may form, creating a 3D connected microfracture network. Moreover, the kerogen body showed 25% and 2% narrowing in bedding-normal direction and bedding-parallel direction after pyrolysis to the wet-gas window (Figure 1.1).

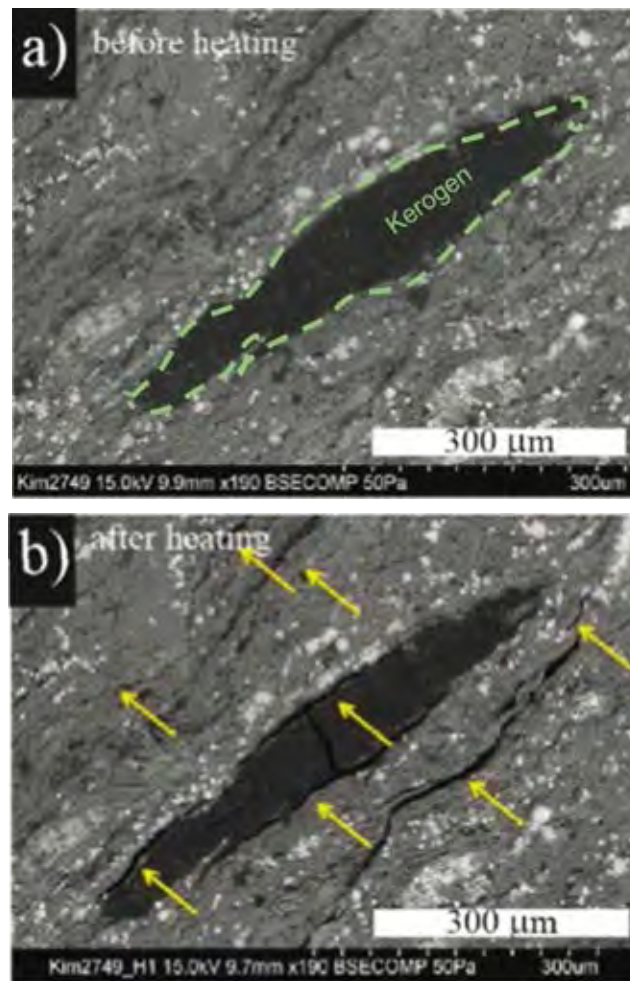


Figure 1.1 Microfracture development related to organic matter maturation (a) before and (b) after a stage of pyrolysis modified from (Allan et al., 2014)

The results are also observed in immature organic-rich Green River shale (TOC=9.92%wt) under time-lapse synchrotron X-ray microtomography by Kobchenko et al. (2011). The

experiment revealed that the cracking occurred at about 350°C and continued propagated parallel to the bedding direction as well as significant mass loss of organic matter. (Figure 1.2)

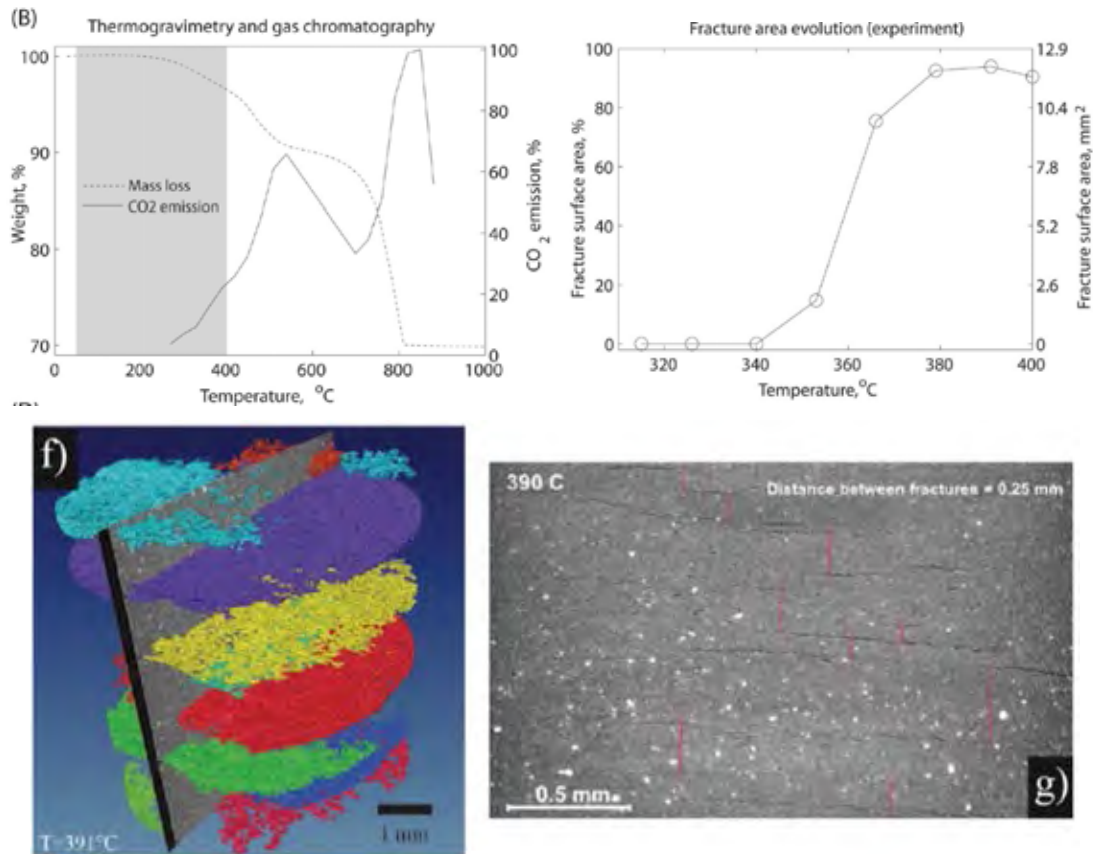


Figure 1.2 The change in total weight, CO₂ emission, and fracture surface area (%) during heating the sample. Synchrotron X-ray microtomography views of a Green River shale that is heated up to 390°C and gas escaping produces a network of crack (Kobchenko et al., 2011; Panahi et al., 2013)

X-ray computed tomography (CT) produces two-dimensional radiographs by measuring the x-ray transmittance of a sample. Those numerous images are used to reconstruct three-dimensional geometry (Rodriguez et al., 2014). High-resolution X-ray CT is a quick and nondestructive technique that is suitable for a wide range of geological investigations (Ketcham et al., 2001). X-ray CT also shows a performance to characterize rock properties such as porosity, density, lithofacies, depositional patterns, rheological characteristics (Jacobs & Cnudde, 2009), or permeability of core rocks and also visualize rock texture including pores, cavities, and cracks (Galkin et al., 2015).

A study by Kanitpanyacharoen et al. (2013) suggests that X-ray Tomography microscopy with Synchrotron light source, the same tool we use in this research, is generally used to produce micrometer-scale images that are useful for characterization three-dimensional microstructure, geometry, and distribution of pyrite and low-density features such as pores, fractures, and kerogen (Figure 1.3).

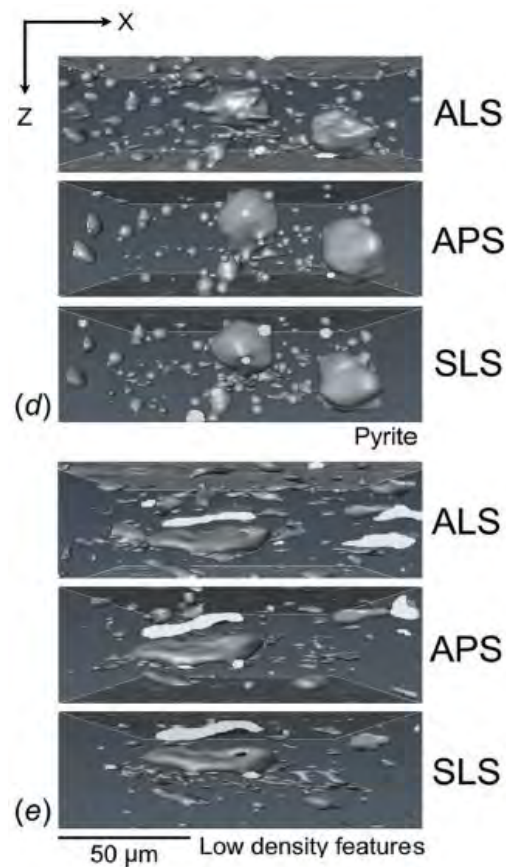


Figure 1.3 The XZ-plane views of the geometry and 3D distribution of (d) pyrite and (e) low-density features from different synchrotron facilities (Kanitpanyacharoen et al., 2013)

1.3 Objective

To quantify the volume fractions and distribution of microcracks and kerogen in shale samples and analyze the orientation and geometry of microcracks and kerogen.

CHAPTER II

GEOLOGY OF STUDY AREA

The Phitsanulok Basin is one of the largest basins of onshore Thailand, extensively covering an area around 10,000 square kilometers (USGS, 2014b). This basin is one of the geologically complex Cenozoic extensional basins (Morley et al., 2001; Morley, 2009) as well as the Fang, Chiang Mai, Mae Sot, Phetchabun, Suphan Buri, and Ayutthaya Basins (USGS, 2014a) (Figure 2.1).



Figure 2.1 Location of the Phitsanulok Basin and other Cenozoic basins in northern Thailand (USGS, 2014a)

2.1 Geological setting

In the Oligocene, the Phitsanulok basin was started to develop in the trend of north-south with extension as a result of to regional strike-slip movement in the Thai-Malay Mobile Belt (a collision zone that is initiated from the Permo-Triassic collision between the

Shan-Thai continental block and Indochina continental block) (Polachan et al., 1991; Bal et al., 1992). The movement is in response to Indian-Eurasian collision during the Himalayan Orogeny that caused intracratonic extensional and transtensional basins (Figure 2.2) developed as a regionally extensive strike-slip system throughout Southeast Asia (Bal et al., 1992) (Figure 2.3). Then the basin was extended significantly to the middle Miocene (Morley et al., 2001) and continued to the upper Miocene with a minor structural inversion during the same period (USGS, 2014b).



Figure 2.2 The Phitsanulok Basin associated with the Uttaradit and Mae Ping fault zones (Flint et al., 1988)

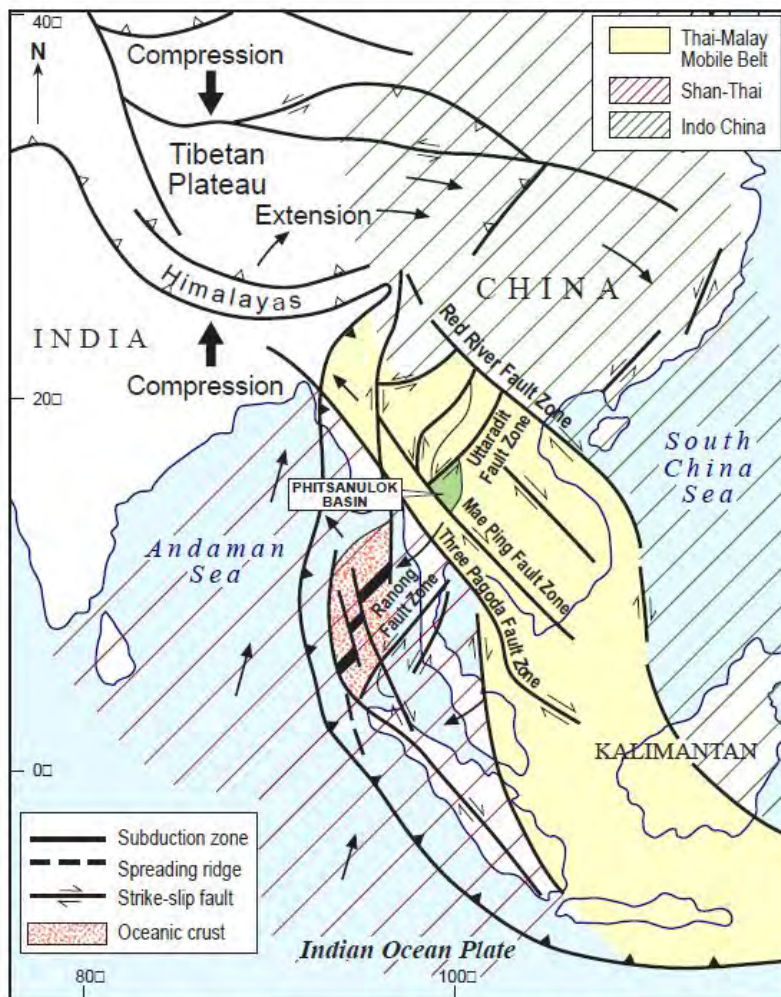


Figure 2.3 Regional tectonic elements and major strike-slip fault relative to the Phitsanulok Basin (Polachan et al., 1991)

The Phitsanulok basin was influenced by four major fault systems, consisting of 1) Uttaradit fault to the north, 2) Phetchabun fault to the east, 3) Mea Ping fault to the south, and 4) Western boundary fault to the west (Thamniyom, 2012). The basin covers the area around 100 km long and 40 km wide at the junction between Uttaradit and Mae Ping Faults (C&C Reservoir, 2009). The western boundary fault which is a normal fault dipping eastward controlled the basin into asymmetric half-graben basin (Thamniyom, 2012) (Figure 2.4).

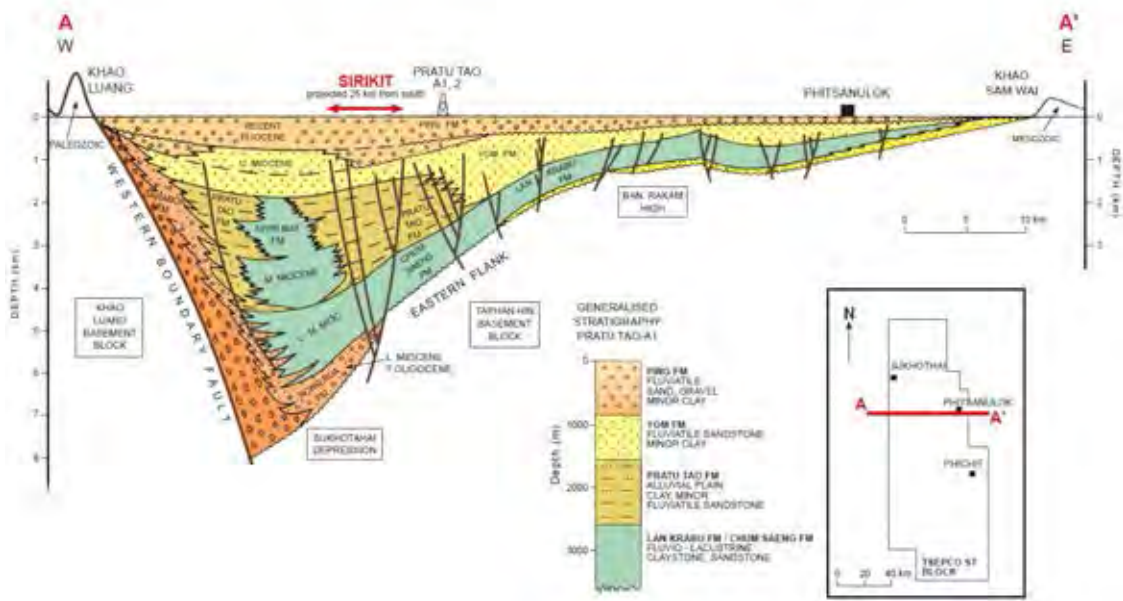


Figure 2.4 W-E cross-section of the Phitsanulok Basin. The asymmetric half graben among Western boundary fault and eastwards pinch-out of sedimentary units (Flint et al., 1988)

Sediments in the basin deposited over the basement of Mesozoic to Paleozoic sedimentary, igneous and metamorphic rocks. The basin is surrounded by highly deformed Mesozoic and Paleozoic sedimentary rocks (C&C Reservoir, 2009). The deepest area adjacent to the western boundary fault, the Sukhothai Depression, became the main basin depocenter with rapid subsidence. Sedimentation rates in the Sukhothai Depression reached up to meter per a thousand years (Bal et al., 1992) and up to 8 km for the total of sediments that have deposited (Flint et al., 1989).

Bal et al. (1992) have subdivided The structural development of the Phitsanulok Basin into four main tectonic phases as follow (Figure 2.5)

Phase I (Late Oligocene to early Middle Miocene): Rapid extension occurred along the Western Boundary Fault. The eastern flank of the basin was presented by smaller antithetic normal faults. Unrestricted strike-slip movement occurred along the Ping, Uttaradit and Phetchabun Fault Systems during this period.

Phase II (early Middle Miocene) Extension continued in the northern, central and southeast parts of the basin. Only in the southwestern Phitsanulok Basin did inversion commence, as sinistral movement on the Ping Fault became blocked.

Phase III (late Middle Miocene) Extension continued in the north and resulted in continued rapid subsidence of the Sukhothai depression. The inversion became more widespread in the south, as a result of the blockage of sinistral movement on the Uttaradit fault zone.

Phase IV (Late Miocene to recent) Dextral movements on the Phetchabun fault became blocked, extensional tectonics ceased, and slow, uniform subsidence took place across the basin. The transpressional tectonic setting of this phase caused a structural inversion, and a system of young dextral faults developed across the Eastern Flank of the basin. Localized basaltic volcanism accompanied this transpressional phase.

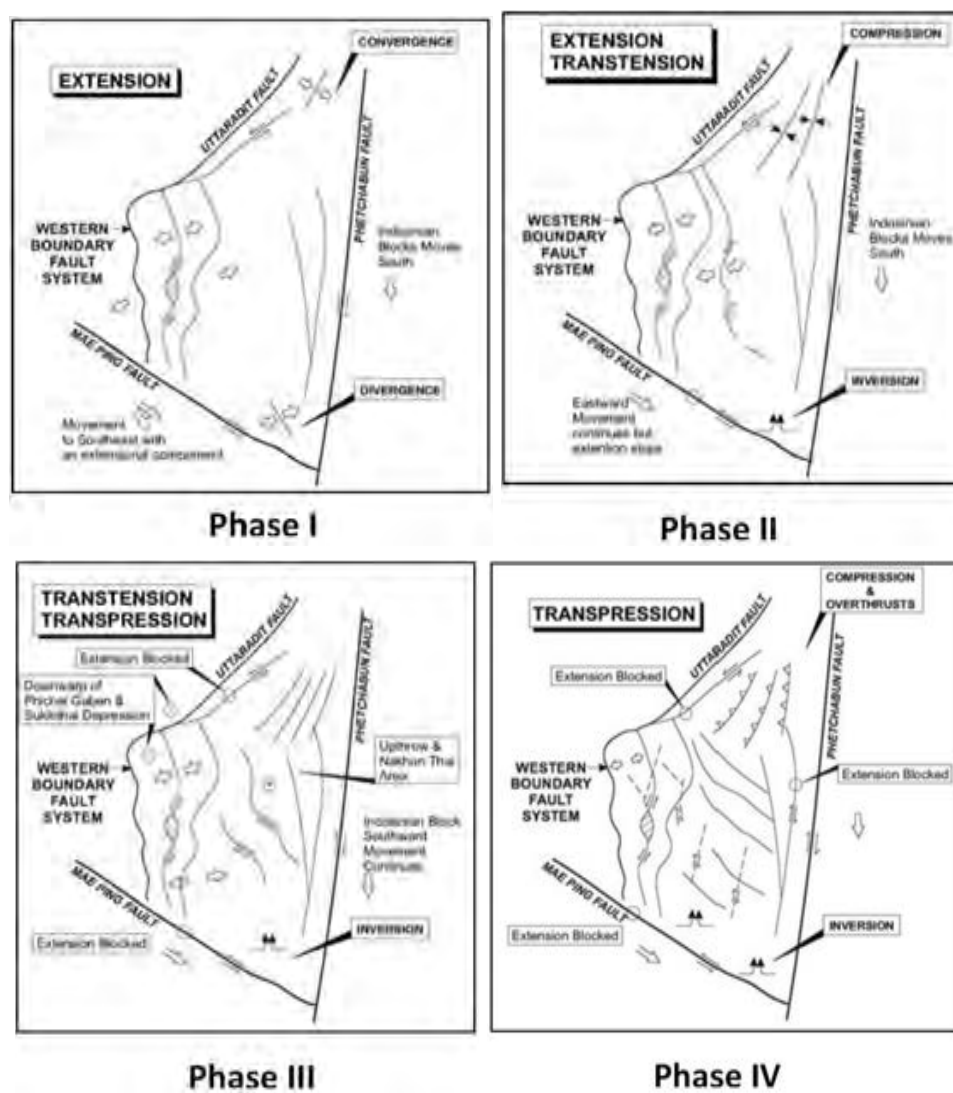


Figure 2.5 The structural development of the Phitsanulok Basin (Bal et al., 1992)

2.2 Stratigraphy and depositional environment

Paleocene to Neogene stratigraphy of the Phitsanulok basin is separated into 5 periods as follow (Figure 2.6).

AGE	FORMATION	THICKNESS (UP TO)	LITHOLOGY	DESCRIPTION	ENVIRONMENT
LATE MIOCENE - RECENT	PING	1,300 m		SANDS/GRAVELS WITH ASSOCIATED CLAYS Sands, clear, white, coarse grained, occasionally gravel. Gravels, variegated, lithic Clays, varicoloured, sandy, silty	Alluvial fans
MIDDLE MIOCENE - LATE MIOCENE	YOM	1,000 m		SANDS/CLAYS Sands, clear, white, coarse grained, occasionally gravel. Clays, varicoloured, sandy, silty	Alluvial plain
	PRATU TAO	1,400 m		SAND (STONES)/CLAY (STONES) Sand (stones), clear, white, fine-coarse grained Clay (stones), redbrown, varicoloured, sandy, silty	Fluvial
EARLY MIOCENE - MIDDLE MIOCENE	LAN KRABU - CHUM SAENG	2,200 m		CLAYSTONES AND SILTSTONES/SANDSTONES Claystones and siltstones, grey, silty, occasionally gastropod-bearing and carbonaceous Sandstones, clear, white, grey, fine-medium grained, thinly bedded	Fluvio-delta & Lacustrine
OLIGOCENE - EARLY MIOCENE	SARABOP - NONG BUA	1,200 m		CLAYSTONES Claystones, redbrown, occasionally grey to varicoloured, with minor coarse-fine lithic sandstones	Alluvial fans & Alluvial plain
PRE-TERTIARY BASEMENT				MESOZOIC - PALEOZOIC CLASTIC, CARBONATE, VOLCANICLASTIC IGNEOUS, AND METAMORPHIC ROCKS	

Figure 2.6 Stratigraphy and depositional environment of the Phitsanulok Basin (Modified from Knox and Wakefield, 1983)

2.2.1 Pre-Tertiary

The basement consists of various types of rock such as Mesozoic - Paleozoic clastic, carbonate, volcanoclastic, igneous, and metamorphic rocks (Smit, 1999; Knox and Wakefield, 1983).

2.2.2 Oligocene - Early Miocene

Sarabop Formation is 1,200 m. thick (DMR, 2014), consisting of immature clastics that deposited in a rift basin along the Western boundary fault (Bal et al., 1992). Sarabop Formation consists of sedimentary rocks such as conglomerate, mudstone, and sandstone that were deposited in alluvial fans (Flint et al., 1988).

Nong Bua Formation is about 1,000 m. thick, consisting of mudstone and sandstone, reddish brown claystone (DMR, 2014). The sediments were accumulated in a low energy alluvial plain (Knox and Wakefield, 1983) and fluvio-deltaic to lacustrine (Flint et al., 1988).

Khom Formation consists of conglomerate, mudstone, sandstone, most parts are quite similar to the Sarabop Formation but deposited in alluvial plain (Flint et al., 1988) of the eastern side of the basin (DMR, 2014) (Figure 2.7).

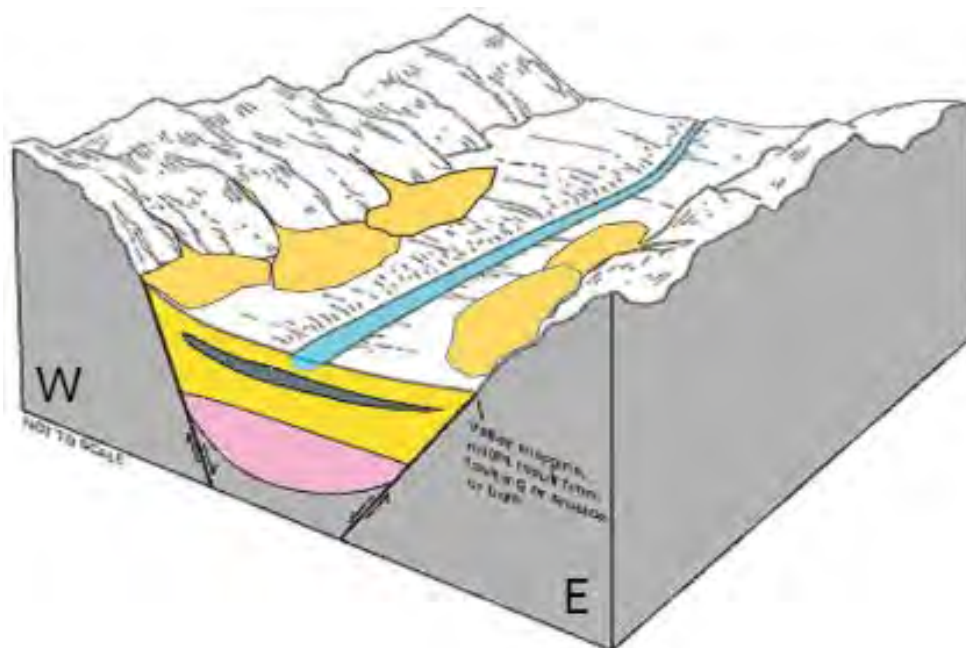


Figure 2.7 Schematic depositional environment of Sarabop Formation, Nong Bua Formation, and Khom Formation (Modified from https://pubs.usgs.gov/ha/ha730/ch_a/gif/)

2.2.3 Early Miocene - Middle Miocene

Chum Saeng Formation is consisting of organic-rich mudstone and claystone and intercalated with coal layers (DMR, 2014). The Chum Saeng Formation was deposited in the depositional environment of lacustrine during the same time as the Lan Krabu Formation. The formation was deposited during a phase of transgression when subsidence rate was high (Bal et al., 1992). This formation becomes a source rock and acts as a seal in the basin. Flow properties within this formation are poor, usually less than 5% porosity and less than 0.01 md of permeability (Pinyo, 2011).

Lan Krabu Formation is about 500-2,200 m. thick, comprising sandstone and interbedded mudstone and siltstone (C&C Reservoir, 2009). Sedimentation occurred between river and lake that are commonly known as fluvio-deltaic environment (Bal et al., 1992). These Lacustrine deltas prograded sediments from north to south (Figure 2.8). Lan Krabu and Chum Saeng formations deposit as cyclic sequences between fluvio-delta and lacustrine environment (Morley and Racey, 2011) (Figure 2.9).

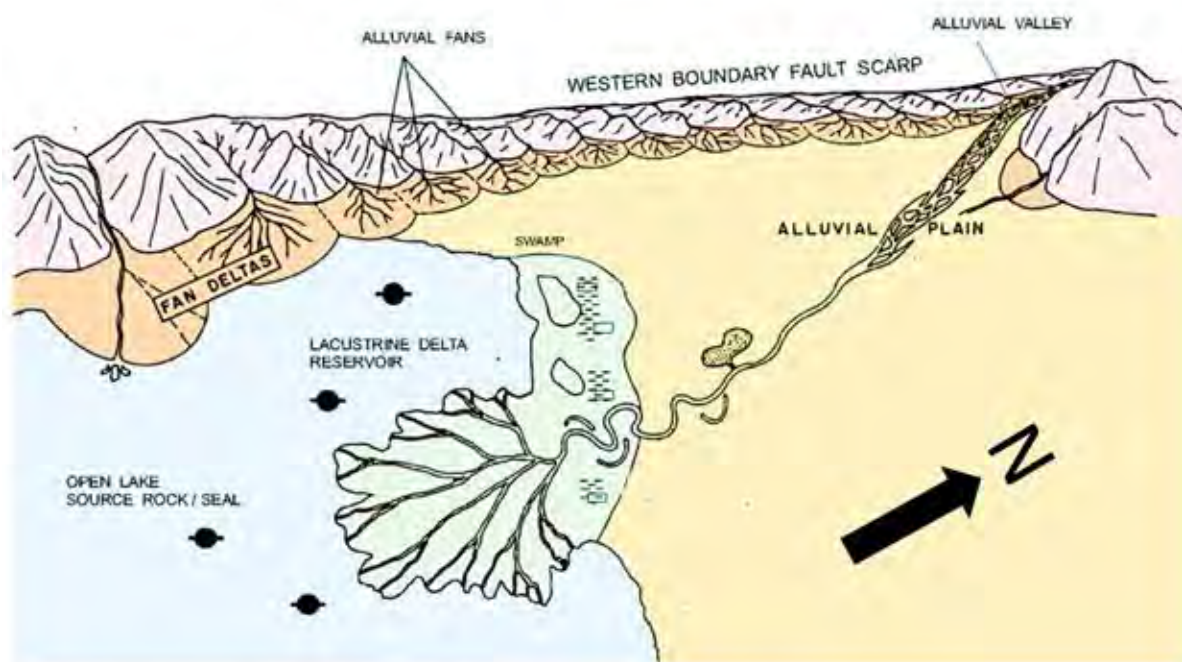


Figure 2.8 Schematic depositional system of Lan Krabu Formation and Chum Saeng Formation (Bal et al., 1992)

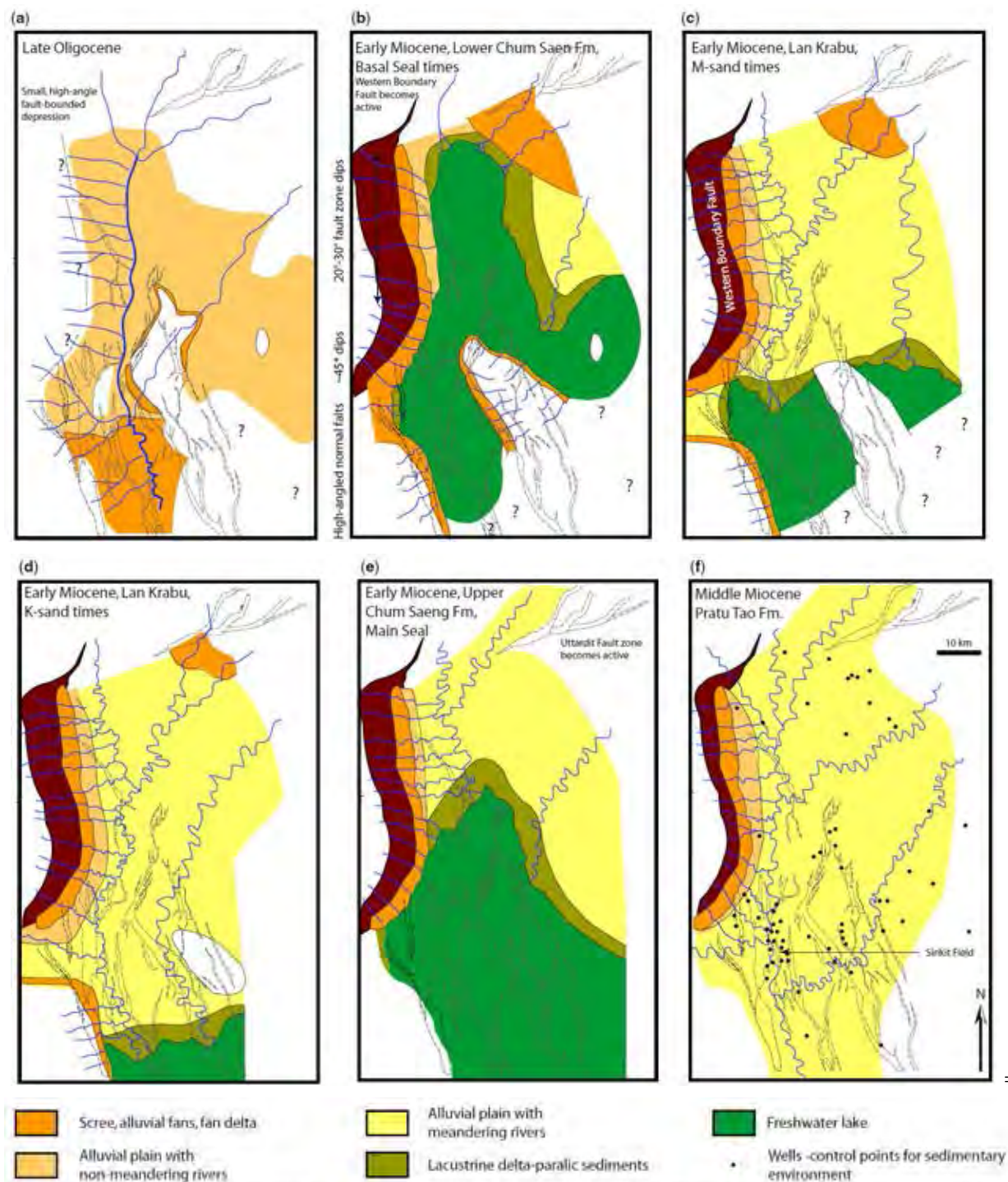


Figure 2.9 Paleogeography of Tertiary sedimentary units of the Phitsanulok basin. (a) Late Oligocene, (b) Early Miocene, Lower Chum Saeng Formation (Basal Seal), (c) Early Miocene, Lan Krabu Formation (M-Sand times), (d) Early Miocene, Lan Krabu, K-sand times, (e) Early Miocene, Upper Chum Saeng Formation (or Main Seal), (f) Middle Miocene, Pratu Tao Formation (Morley and Racey, 2011)

2.2.4 Middle Miocene - Late Miocene

Pratu Tao Formation is about 1,400 m. thick, accumulated in an alluvial environment (Bal et al., 1992) consisting of mudstone intercalated with sandstone (DMR, 2014).

Yom Formation is about 1,000 m. thick, dated as Middle Miocene to Recent. Sedimentation occurred in an alluvial plain environment. It's comprised of coarse to very coarse-grained sandstone with brown to reddish brown mudstone and some coal (DMR, 2014).

2.2.5 Late Miocene - Recent

Ping Formation is over 1,200 m. in thickness and dated as Late Miocene to Recent. Sedimentation occurred along a piedmont zone in alluvial fans. It mainly consists of sand and gravel intercalated with reddish brown and yellow clay with some coal (DMR, 2014).

2.3 Petroleum system

2.3.1 Source rock & Maturation

The source rocks are up to 50-400 m. thick (Pinyo, 2011) and belong to the Early to Middle Miocene Chum Saeng Formation. Coals are also presented locally. Freshwater and terrestrial palynofacies and freshwater gastropod fossils confirm the lacustrine origin of the source rock (C&C Reservoir, 2009). This formation becomes a source rock and acts as a seal in the basin. Kerogen is mainly Type I derived from freshwater algae and Type III from higher plants (C&C Reservoir, 2009) with a TOC value ranging from 5-20% (Boonyasatphan, 2017). Petroleum in the basin was generated from the kerogen within the shales (Lawwongngam and Philp, 1993). The formation is thermally mature (more than 0.55 percent Ro) and overpressured (greater than 0.45 pounds per square inch per foot, psi/ft) (USGS, 2014a). Source kitchens occur in the deepest part of the basin, north of the field. The oils are relatively immature, have not been bio-degraded and are low in aromatics. Variations in isotopic ratios between different oil pools may reflect sourcing at different stages of source rock maturation, while similarities in chromatograms indicate common source and migration histories (Lawwongngam and Philp, 1991). Oil generation may have commenced in the Pliocene in the west of the basin, where heat flow is high. Generation and expulsion may have taken place at a depth >4 km (Knox and Wakefield, 1983) (Figure 2.10).

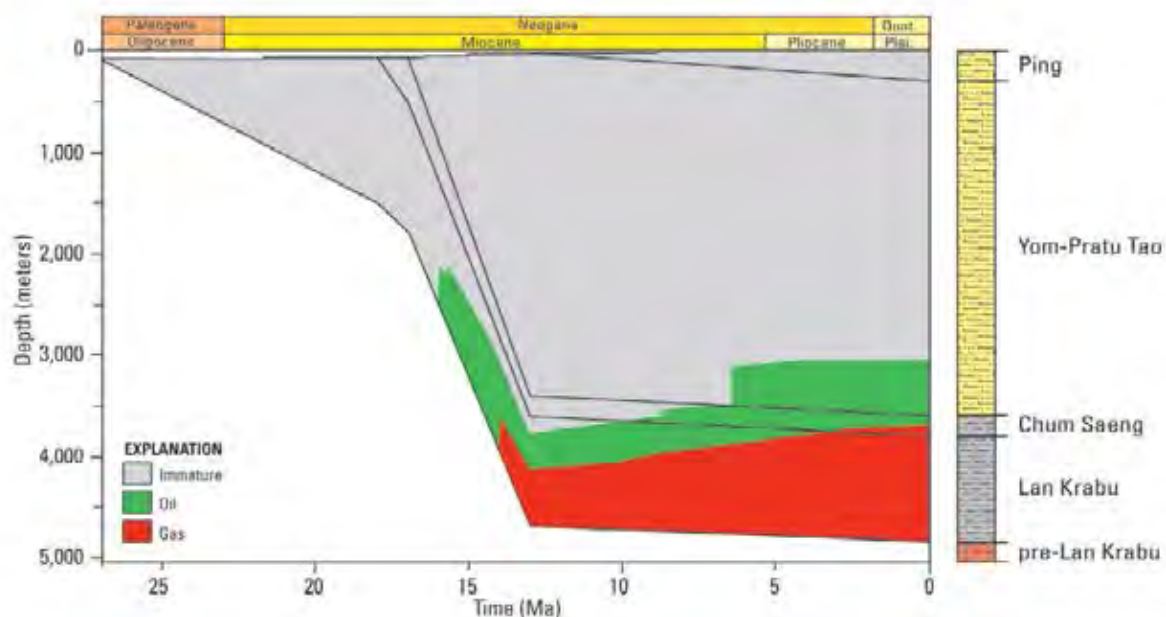


Figure 2.10 1D petroleum system modeling from well SBP-A01 shows burial history of Chum Saeng Formation source rock and hydrocarbon generation. (USGS, 2014b)

Besides, Knox and Wakefield (1983) described properties of the oil which was migrated to the Sirikit Field as following (Table 2.1).

Table 2.1 Basic properties of Sirikit oil (Knox and Wakefield, 1983)

Properties	Range
API gravity	38.2 - 41.2
Flash point (°F)	80 - 98
Kinematic viscosity (at 122 °F)	4.5 - 11.35
Paraffin wax content (% wt)	14.5 - 20.8
Pour point (°F)	+90 - +95
Asphaltenes (% wt)	0.05 - 0.1
Sulfur (% wt)	0.15 - 0.38

2.3.2 Reservoir

Deltaic sandstones of the Lan Krabu Formation sealed by lacustrine claystones of the Chum Saeng Formation. Lan Krabu formation and Chum Saeng formation are the main reservoirs/seal pairs due to cyclic delta progradation and lacustrine transgression. Reservoirs in this formation are separated into 4 main units. These are “D”, “K”, “L”, and “M” sands respectively from youngest to oldest (Bal et al., 1992) (Figure 2.11). Individual sand bodies can be found as continuous distributary mouth bars and discontinuous channel sand with less than 7 m thick and 2-3 km lateral extent (Flint et al., 1988).

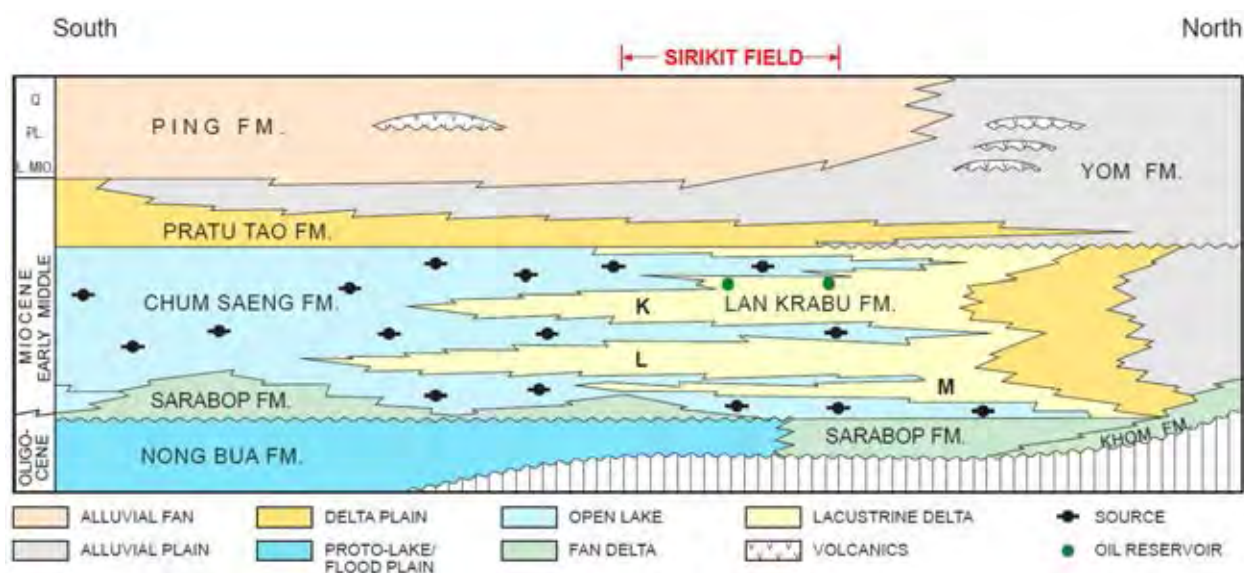


Figure 2.11 Schematic stratigraphy of sedimentary units across the Phitsanulok Basin from north to south. Lan Krabu Formation are separated into subunit due to interfingering of the formation and Chum Saeng Formation (Ainsworth et al., 1999)

Potential reservoirs also occur in fluvial sandstones of the Middle Miocene Pratu Tao and Yom Formations. These formations have fair to good reservoir properties as the Lan Krabu Formation but less in continuous and thick seals. Vertical migration is required to charge the reservoir. Therefore, Pratu Tao and Yom Formations becomes a less potential reservoir (Bal et al., 1992).

Pre-Tertiary basement consisting of sedimentary, metasedimentary and volcanic strata may constitute fractured reservoir in buried hill traps. The basement is sealed by Tertiary claystones. This type of petroleum play has encountered good oil production in the Sirikit field (Bal et al., 1992).

Unconventional reservoir rock is represented by Chum Saeng formation. The oil and gas are thermally mature from Chum Saeng formation. The formation has considerable porosity and low permeability. Fractures produced during hydrocarbon generation may improve the reservoir properties such as porosity and permeability (Pinyo, 2011).

2.3.3 Seal

The Chum Saeng Formation is the top seal and lateral seal to hydrocarbon accumulations in main reservoir. Thinner lacustrine shales in the Lan Krabu Formation act as intra-formational seals. These seal separate different reservoir zones within the reservoir (Morley and Racey, 2011). Pratu Tao Formation is intercalated with ephemeral lacustrine clays which are thin and low continuity. The Tertiary claystones acted as seal for Pre-Tertiary basement.

2.3.4 Trap

Hydrocarbon accumulations in the Phitsanulok basin are dominantly controlled by the complex fault patterns. Tilted fault blocks in some field are dissected into many compartments by intense wrench-related faulting. Clay smear along the fault affects fault sealing potential that is allowing the accumulation of hydrocarbon. Fault juxtaposition of reservoirs and interbedded claystones can trap only limited hydrocarbon column. The stratigraphic traps such as onlap, pinch out, buried hill are commonly found in the basin (Bal et al., 1992).

2.3.5 Migration

Source rock becomes mature locally in the northern part of the basin. The main source rock reaches into a gas window within the central Sukhothai Depression, and into oil window on the flank (Figure 2.12). The hydrocarbon show in the basin indicates the occurrence of migration. Lateral migration is predominantly between time-equivalent formations, Chum Saeng and Lan Krabu. Vertical migration may occur along fault planes, especially in reactivated faults. On the eastern flank is a shadow zone for hydrocarbon because north-south faults block eastward-migration (Bal et al., 1992).

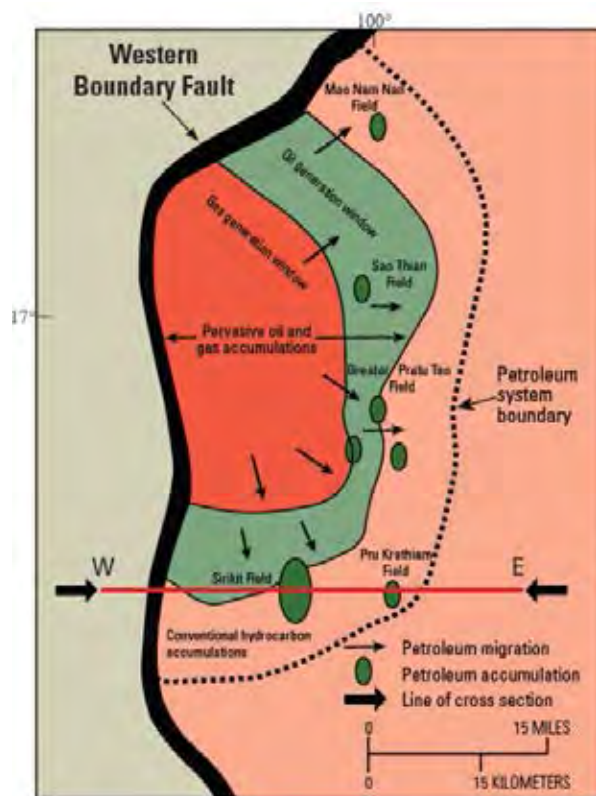


Figure 2.12 Schematic map shows the boundary of the petroleum system and maturity of Chum Saeng Formation under Sukhothai depression (Pinyo, 2011)

CHAPTER III

METHODOLOGY

The methodology is separated into three steps; (1) Sample preparation, (2) Measurement by Synchrotron X-ray micro-computed tomography (Syn-MCT) and, (3) Data analysis by Avizo Fire. Syn-MCT is used to carry out data from each component based on linear absorbance. Then, the Avizo Fire software is used as a quantification tool to produce three-dimensional visualization, segmentation and to characterize geometry, the volume fraction and distribution. This high-resolution 3D imaging technique is used to provide details on shale samples, especially, microcrack and kerogen.

3.1 Sample preparation

Three shale samples are collected from the Phitsanulok Basin. Samples are obtained by core drilling in the same borehole. The conventional cores are cut into a small cylindrical plug for analysis. Samples are cut into a smaller size due to the analysis of micro-scale features. Each sample is cut into rectangular prism then polished into a small cylinder with a diameter of 1 mm and a thickness of 1 cm for the experiment.

3.2 Synchrotron X-ray micro-computed tomography (Syn-MCT) imaging technique

In this study, the tomographic imaging technique is performed with a synchrotron light source. The synchrotron light source provides a high energy beam of X-ray that travels around a particle accelerator. The magnetic fields are used to bend the particle beam into a cyclic-closed path to accelerate particle velocity (Figure 3.1). The kinetic energy is increased until it is enough for the experiment.

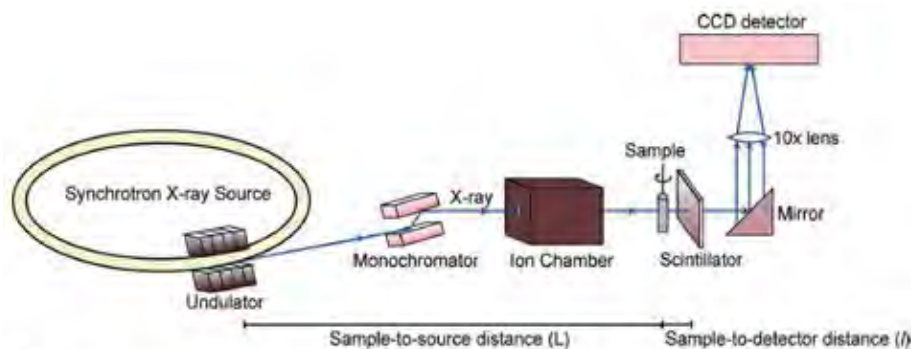


Figure 3.1 Schematic diagram of Synchrotron X-ray micro-computed tomography (Syn-MCT) equipment (Kanitpanyachoen et al., 2013)

First, bright-field image and dark-field images are collected for x-ray fluctuation noise-removal and background normalization before the data from samples are collected. Then, the cylindrical sample is mounted on a rotation stage vertically to the long axis. Each sample is rotated in 0.120° incremental steps for a total of 180°. During the rotation, the monochromatic X-ray energy of 18 keV is beamed through the samples. The x-ray beam is absorbed by materials as a function described by Beer-Lambert's law. (Equation 3.1)

$$\frac{I}{I_0} = 10^{-\alpha l} \quad \text{-----(Equation 3.1)}$$

where I is light intensity after transmitting the material, I_0 is light intensity beamed from the light source, l is path length that X-ray pass through the sample, and α is the absorption coefficient of the material. (Figure 3.2)

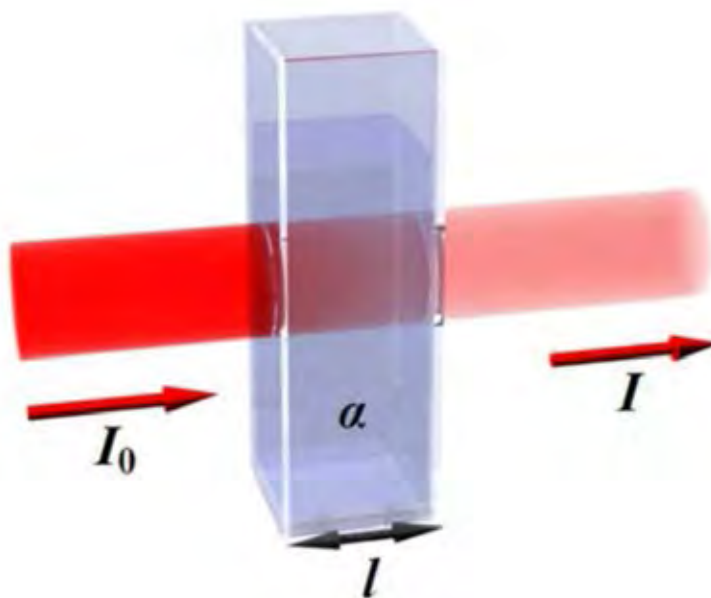


Figure 3.2 Beer-Lambert's law shows the relationship between intensity of light and the material's absorption coefficient (www.chegg.com)

The result of different coefficient, which depends on the density and an atomic number of elements in chemical molecules, is showed in transmitted X-ray intensity. The transmitted X-ray intensity was absorbed by a thin scintillator screen, which converts X-rays to a certain wavelength of visible light. The visible light was further projected onto a CCD detector and

creates two-dimensional grayscale X-ray attenuation map. A bright area in the map represents high atomic number materials, while lower atomic and low-density materials are shown by a dark area.

Then, the x-ray attenuation map is quality-corrected by several processes as following (Figure 3.3); noise removal which effected X-ray fluctuation by Equation 3.2

$$I_c = (I_s - I_d)/(I_b - I_d) \quad \text{-----(Equation 3.2)}$$

where I_c is the corrected image, I_b is the bright-field image, I_d is the darkfield image and I_s is the raw projection image (Wang et al., 2001).

Normalization is processed by choosing areas of the corrected images with no data then replace with an average value. After that, rearrange data into a sinogram which contains information of all projection angles of a horizontal line. Finally, the data are reconstructed by an algorithm and represented in 32-bit TIF format with 2048 x 2048 in pixels size.

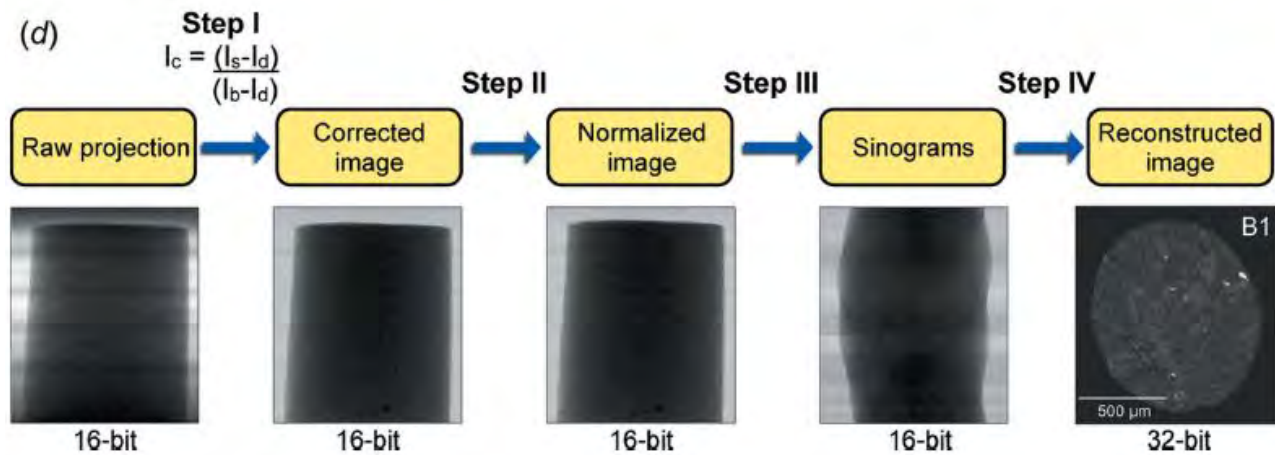


Figure 3.3 Data reconstruction workflow of Barnett shale sample (Kanitpanyachoen et al., 2013)

3.3 Data analysis

Tool for 3D tomographic data analysis used in this research is Avizo Fire software. Several processes and tools are further used as shown in Figure 3.4. A number of 2D images are chosen from the interval of the least error data set to render a 3D volume. All data are set a pixel size corresponding to the synchrotron facility. The total volume is cropped into a smaller

volume that can be processed smoothly in the software. The brightness of the raw image is adjusted through the Normalize grayscale tool to range the value from 0 to 255. Then, noises are removed with a 3D median filter (Figure 3.5) by replacing a voxel with a median of surround voxel.

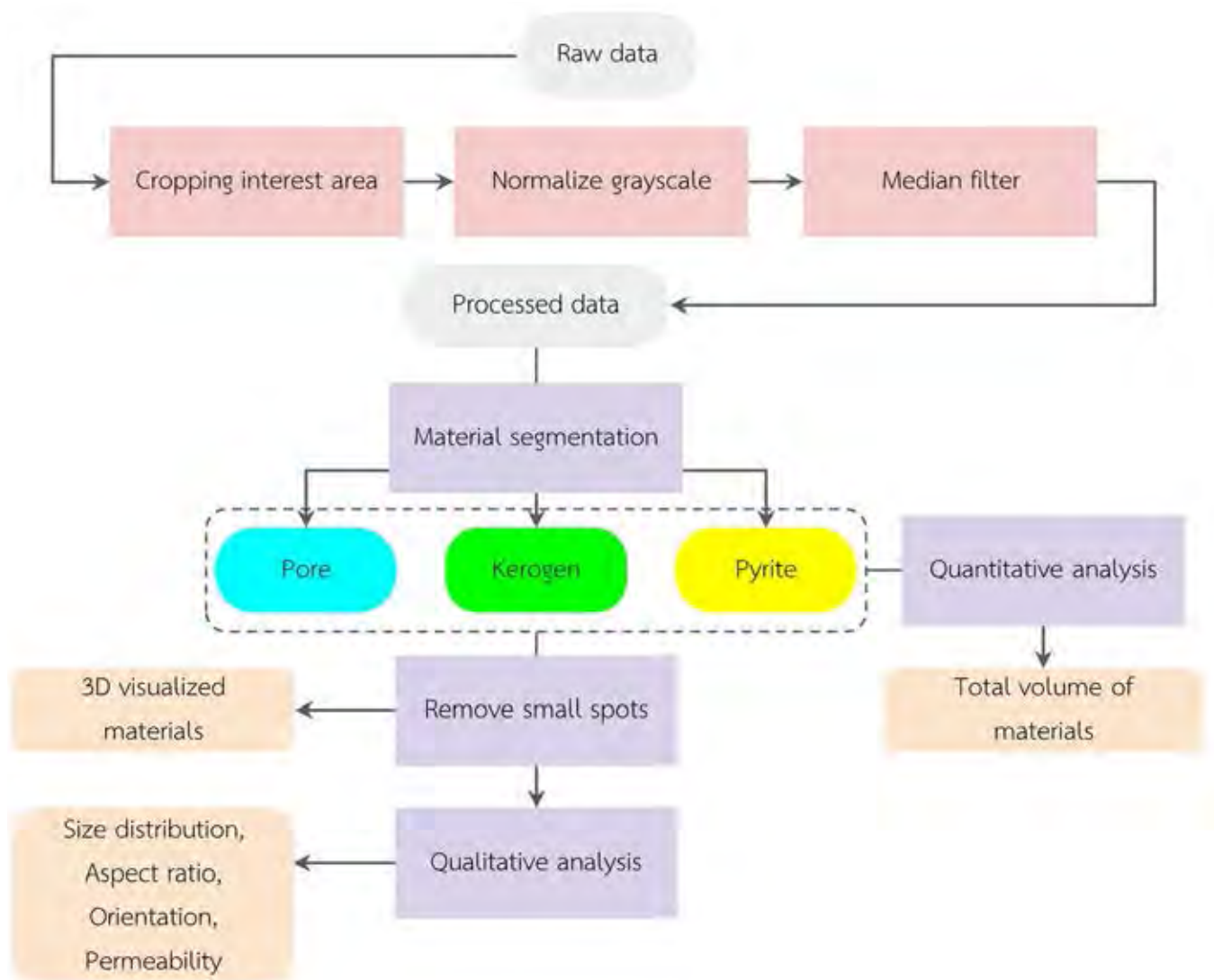


Figure 3.4 Workflow of data analysis processing

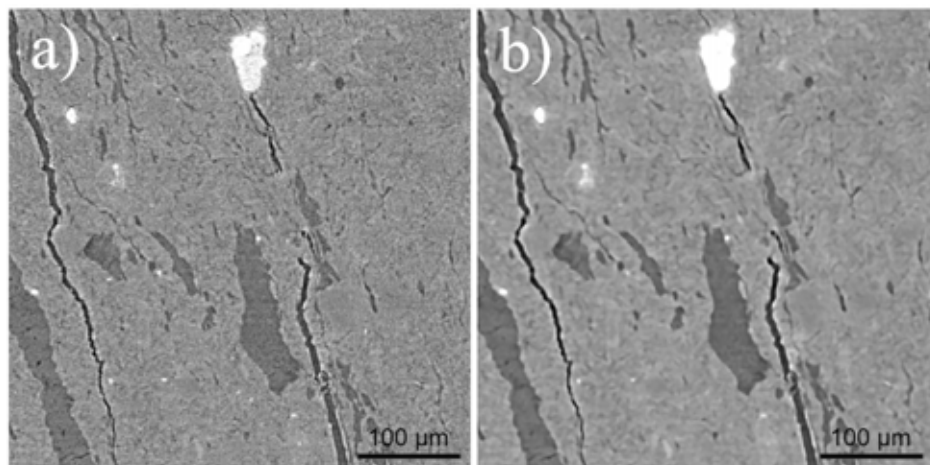


Figure 3.5 a) noise can be observed in a raw image before 3D median filter b) image after 3D median filter

Distinctive components are segmented by selecting the threshold of grayscale based on Beer-Lambert's law assuming that the high-absorbing component (bright) is pyrite. While the low-absorbing component (quite dark) represent low-density material which is kerogen. The lowest-absorbing component (dark) are pore and microcrack. (Figure 3.6)

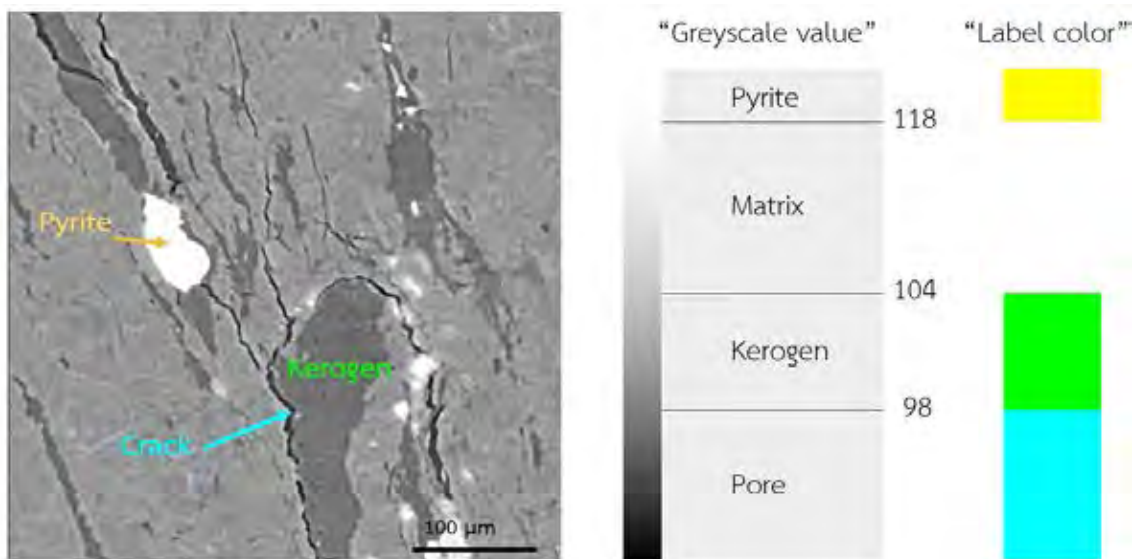


Figure 3.6 Component classification on grayscale shows the high-absorbing component (bright) is pyrite, the low-absorbing component (quite dark) is kerogen, The lowest-absorbing component (dark) are pore and microcrack

Then, several functions are used for proper analysis. “Material statistics” is used to obtain a total volume of segmented materials. The 3D segmentations are further processed with “Remove small spot” function as shown in Figure 3.7. The function can significantly reduce the number of isolated micro-to-nano pores in order to preserve only connected components (e.g. microcracks, kerogen). The geometry and volume of microcracks and kerogen can thus be clearly separated from those of pores. The total volume of microcrack before and after remove isolated pores are shown in Table 3.1. After processing “Remove small spots”, porosity is reduced by 0.26% and these isolated pores do not affect connectivity and fluid flow. “Label analysis” is further used to obtain specific data such as amount and volume, aspect ratio, and orientation of each isolated material.

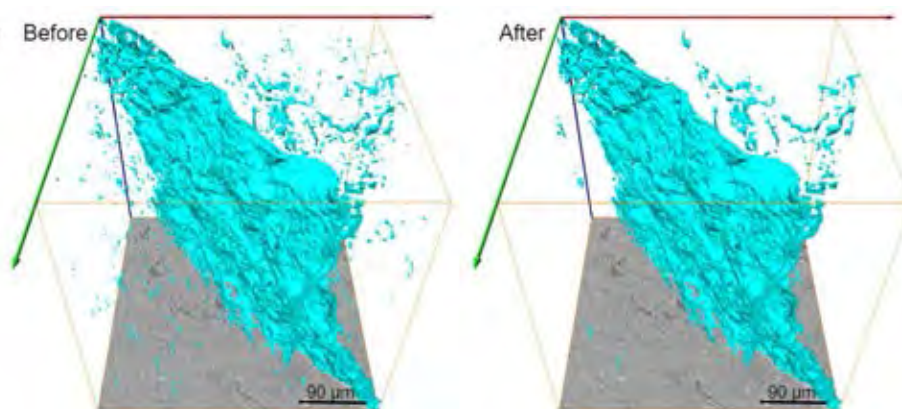


Figure 3.7 3D segmentation of microcracks in sample PHS02-3 before (left) and after small spots removal (right)

Table 3.1 Volume of cracks comparison after processing “Remove small spots” in PHS02-3

Parameters	PSH02-3	PSH02-3 with "Remove small spots"
Volume max. (μm^3)	1,000,130	1,000,130
Volume Min. (μm^3)	0.37	384.45
Total microcrack volume (μm^3)	1,191,959.31	1,067,036.20
Porosity (%)	2.55	2.29 (-10.2%)
Isolated nanopores	5,975	68 (-98.9%)

CHAPTER IV

RESULTS

Two shale samples (PHS01 and PHS02) from the Phitsanulok basin are analyzed with x-ray microtomography technique. Due to a massive amount of data per sample (~20 GB), the samples are randomly divided into four small cubes to allow fast 3D segmentation and processing time. A total of subsamples are investigated for geometry and distribution of microcracks and kerogen in this study. Each cube, known as volume of interest (VOI), has a volume of $360 \times 360 \times 360 \mu\text{m}^3$.

4.1 2D observations

2D reconstruction images from x-ray microtomography technique were used due to some micro-scale features are easier to observe clearly under the high-resolution 2D image (raw image before using “Median filter”). Basic features were distinguished from 2D slices on XY, XZ, and YZ planes of VOIs for quantitative analysis. These features were characterized on elementary materials such as pore, kerogen, and pyrite inside VOIs by its visible geometry, size, and distribution. Samples of 2D images are shown in figure 4.1 (a) - (l)

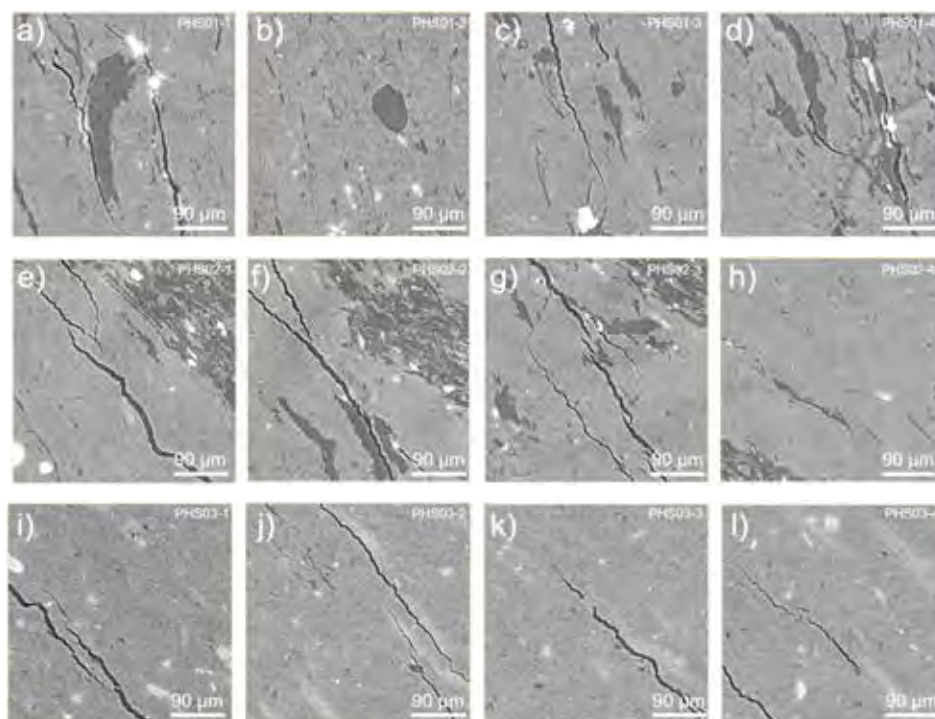


Figure 4.1 2D reconstruction images from all VOIs such as a-d) PHS01-(1,2,3,4), e-h) PHS02-(1,2,3,4), i-l) PHS03-(1,2,3,4)

Features that we mentioned in the 2D analysis are expected to be significant as they can be likely controlled by compaction, depth of burial, and maturation. Features were simply classified as various type of pores, according to Loucks et al. (2012). These pores are divided into interparticle pores, intraparticle pores, organic-matter pores, and fracture pores (microcracks) (Figure 4.2). Intraparticle were generally present as pores within pyrite framboids (Figure 4.2) and fossil bodies (Figure 4.3) in PHS01 and PHS03. Intraparticle, especially pores within clay aggregates might be present in all samples as shale is commonly composing of clay mineral but the resolution is poor to observe these clay's platelets. Interparticle pores were present in all samples (Figure 4.4). Organic-matter pores were presented obviously in PHS01 and slightly ambiguous in PHS02 due to the smaller size and amount of them (Figure 4.5). Perpendicular cracks, bedding-normal direction crack on kerogen patch, were found in PHS01 and PHS02 (Figure 4.6). Additionally, bedding-parallel direction cracks on the edge of kerogen body (Figure 2) were observed in this research. These kerogen-edge cracks were present in all samples, but densely in PHS01 and PHS02. Existence of these features is shown in Table 1.

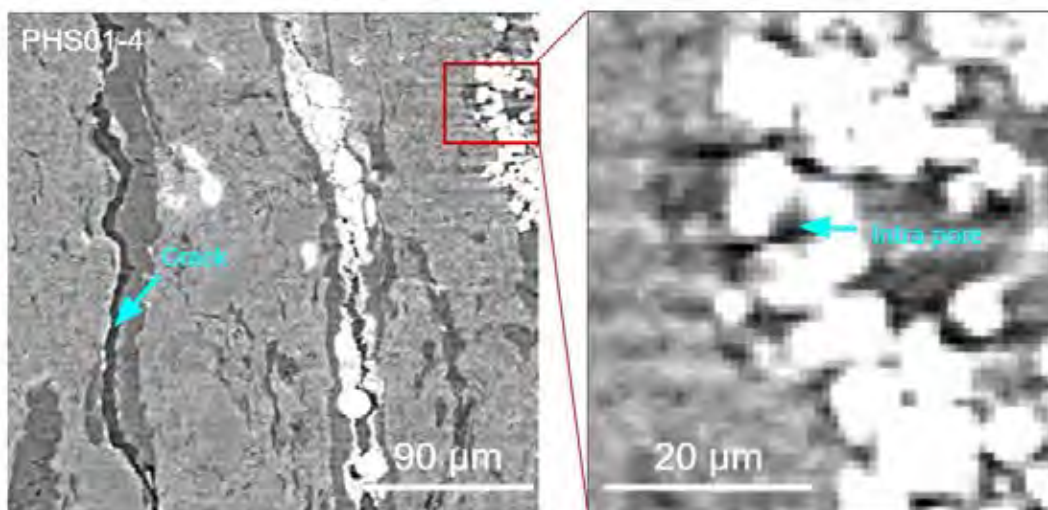


Figure 4.2 2D image of PHS01-4 shows fracture pore (crack) which is parallel to kerogen patch and pyrite framboids with its intraparticle pore

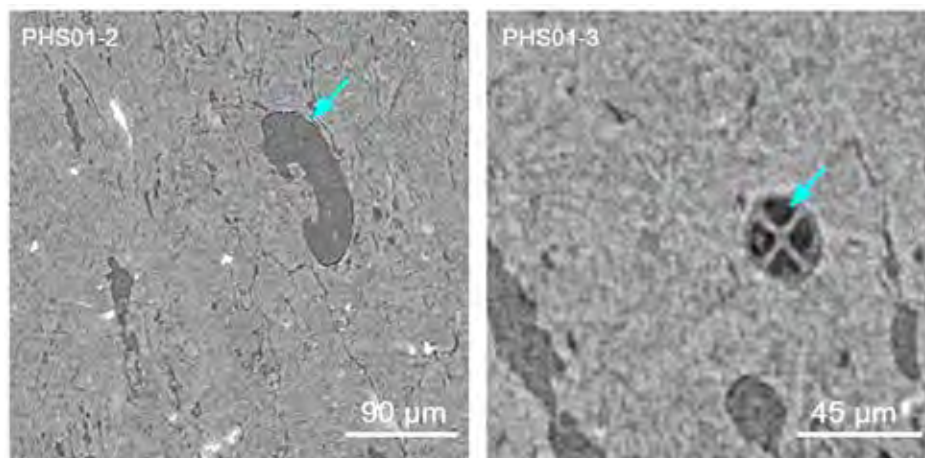


Figure 4.3 2D images of PHS01-2 and PHS01-3 show fossils trace with pores in fossil bodies

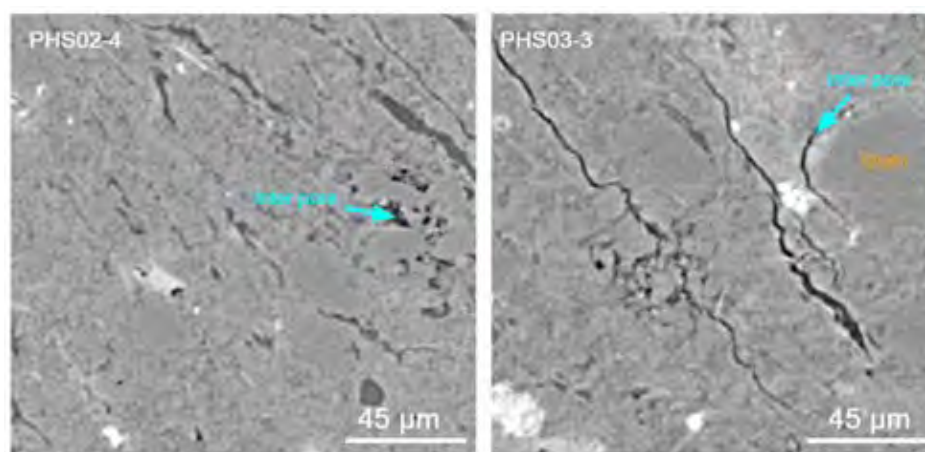


Figure 4.4 Pores between grains are shown in PHS02-4 and PHS03-3 and pore at the edge of rigid grain is shown in PHS03-3

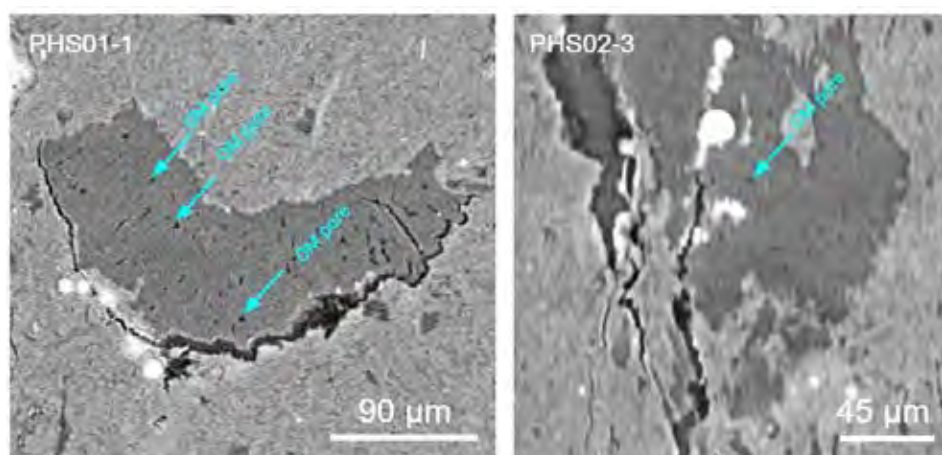


Figure 4.5 Organic-matter pores are shown obviously with the larger size in PHS01-1 comparing to organic-matter pores in PHS02-3

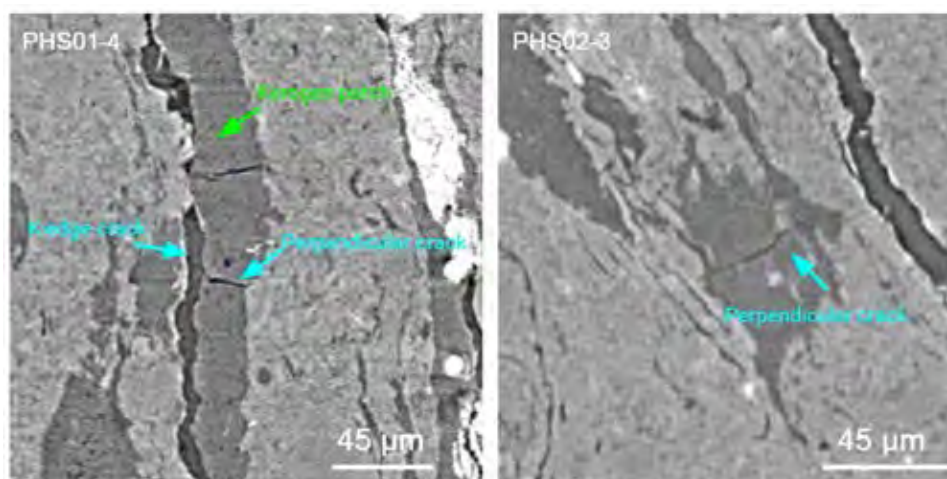


Figure 4.6 Perpendicular cracks are present on the kerogen patch of PHS01-4 and PHS02-3

Table 4.1 Conclusion of features present in sample PHS01, PHS02, and PHS03

Feature \ Sample	PHS01	PHS02	PHS03
Interparticle pores	✓	✓	✓
Intraparticle pores	✓	-	✓
Framboidal pyrites	✓	✓	✓
Organic-matter pores	✓	✓	-
Perpendicular cracks	✓	✓	-
Kerogen-edge cracks	✓	✓	✓
Fracture pores (cracks)	✓	✓	✓

Abundant
 Rare
 Absent

4.2 Volume fractions and size distributions

Materials were reconstructed from selected small voxels to create their large volumes. Volumes were separated from each other and can be individually analyzed certain data such as volume, orientation, surface area, width, and length. A few VOIs of 3D segmented volumes from

PHS01, PHS02, and PHS03 are shown in Figure 4.7. Materials we focused on in this research are illustrated in different colors, pore (cyan), kerogen (green), and pyrite (yellow).

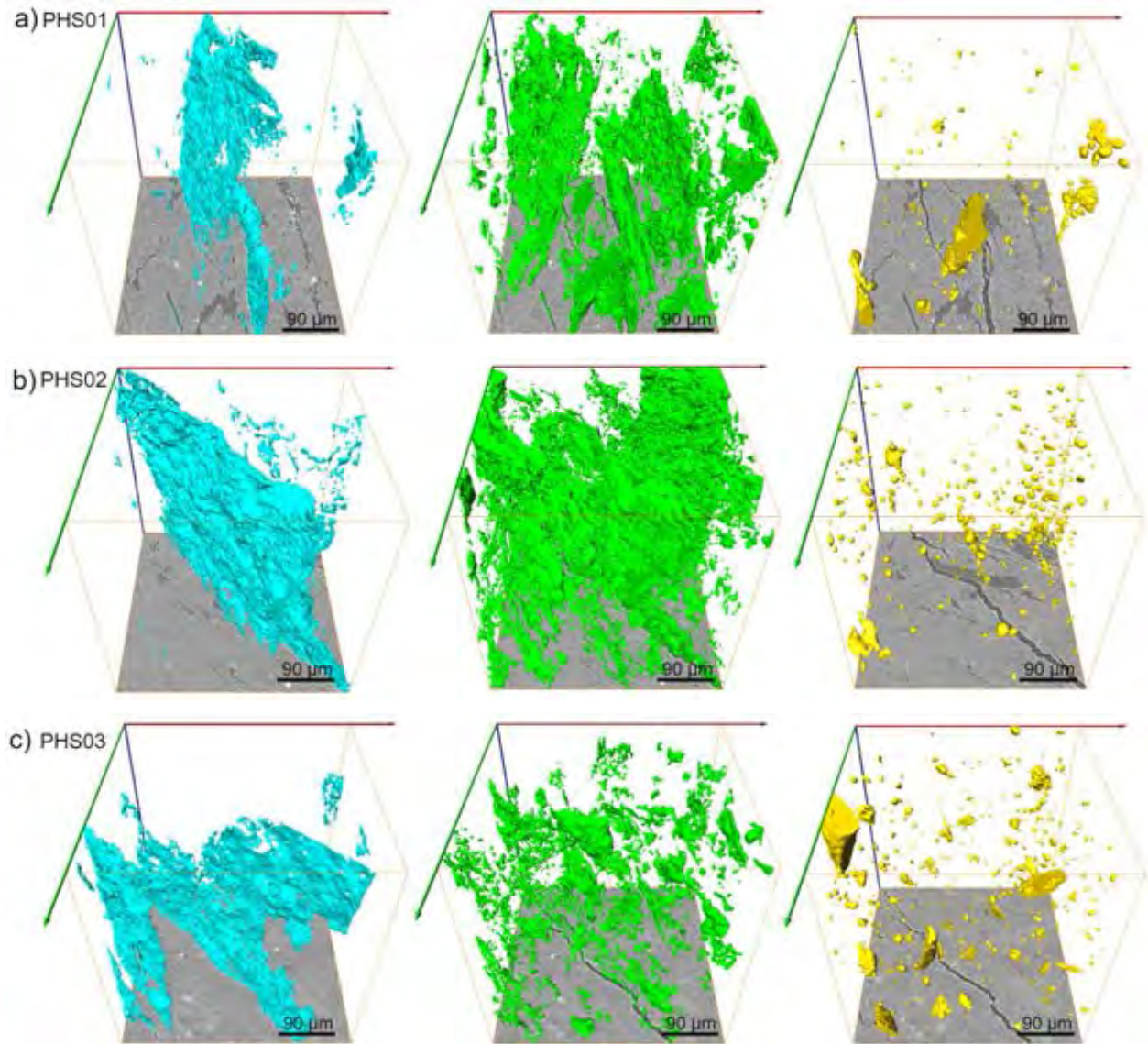


Figure 4.7 3D segmentation of pore (cyan), kerogen (green), pyrite (yellow) were illustrated from PHS01-3, PHS02-3, and PHS03-4

Porosity and volume of kerogen and pyrite in each VOI from PHS01, PHS02, and PHS03 samples are shown in Table 2. The average porosity of PHS01, PHS02, and PHS03 are 1.47%, 1.98%, and 1.12%. The average percent of kerogens are 10.60%, 12.97%, and 1.93%. The

average percent of pyrite are 1.16%, 0.57%, and 1.07% respectively. The volume percent of kerogen and pore are displayed in the scatter plot shown in Figure 4.8.

Table 4.2 Quantity of pore, kerogen, and pyrite of PHS01, PHS02, and PHS03 in volume%

Samples	VOIs	Porosity(%)	Kerogen(%)	Pyrite(%)
PHS01	PHS01-1	1.83	13.83	1.80
	PHS01-2	0.52	7.01	0.62
	PHS01-3	1.70	7.58	0.56
	PHS01-4	1.82	13.99	1.67
Average (S.D.)		1.47 (0.63)	10.60 (3.83)	1.16 (0.66)
PHS02	PHS02-1	2.38	12.90	0.51
	PHS02-2	2.55	19.07	0.88
	PHS02-3	2.55	11.32	0.45
	PHS02-4	0.44	8.58	0.45
Average (S.D.)		1.98 (1.03)	12.97 (4.44)	0.57 (0.21)
PHS03	PHS03-1	1.49	2.15	1.01
	PHS03-2	1.13	1.85	1.87
	PHS03-3	0.81	1.75	0.56
	PHS03-4	1.06	1.97	0.83
Average (S.D.)		1.12 (0.28)	1.93 (0.17)	1.07 (0.57)

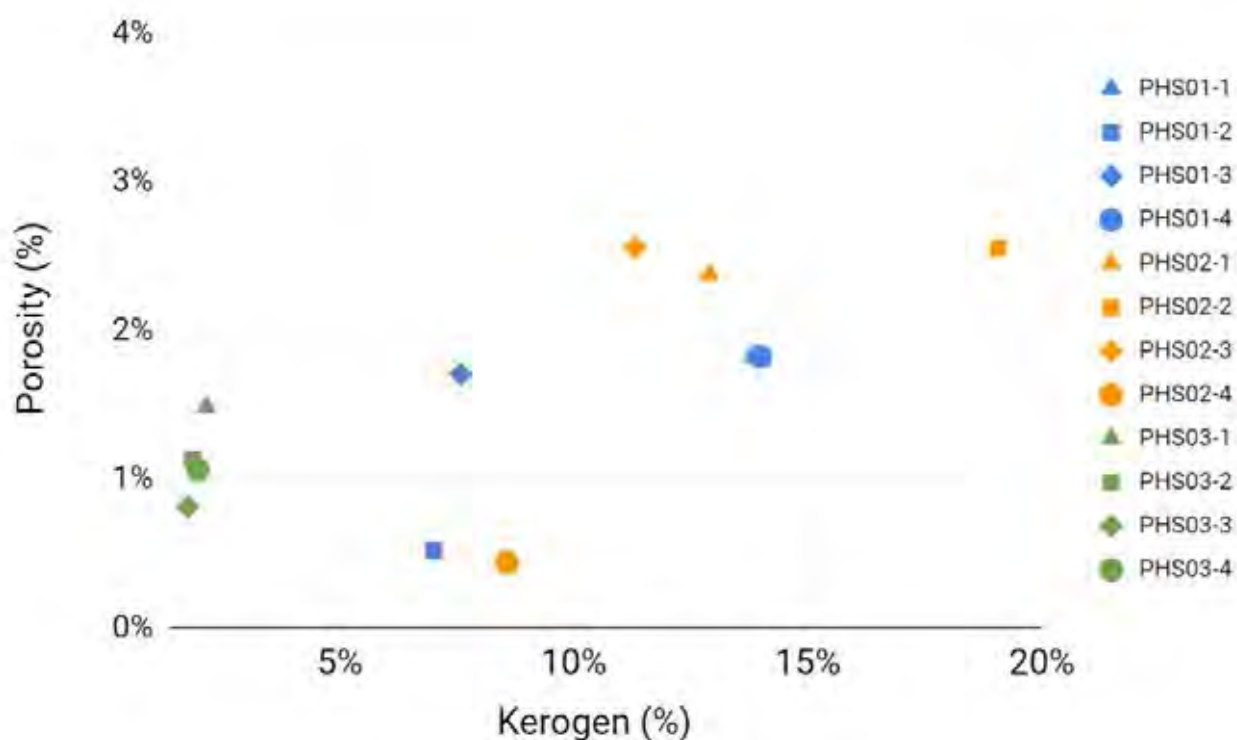


Figure 4.8 Scatter plot between porosity and kerogen (percent by volume) of each VOI

In addition, a volume histogram and cumulative volume percentage of microcracks and kerogen are plotted as shown in Figure 4.9. Most kerogens are in the approximate range of 300 to $10^6 \mu\text{m}^3$ that are calculated for 25% of the total amount. The rest 75% of the total volume is dominated by small numbers of outliers that hold larger volumes than $10^6 \mu\text{m}^3$. But it is the exception for PHS03 because of a little amount of kerogen it has. The range of pore is typically smaller, less than 20% of the total volume is made up from 300 to $10^5 \mu\text{m}^3$ pore. However, it also shows the influence of larger crack involving the total volume the same as kerogens. In conclusion, the number of pores and kerogens are more in a smaller size and become decreasing when the size increases. Most of the volume comes from larger connected materials although it does not have a large number.

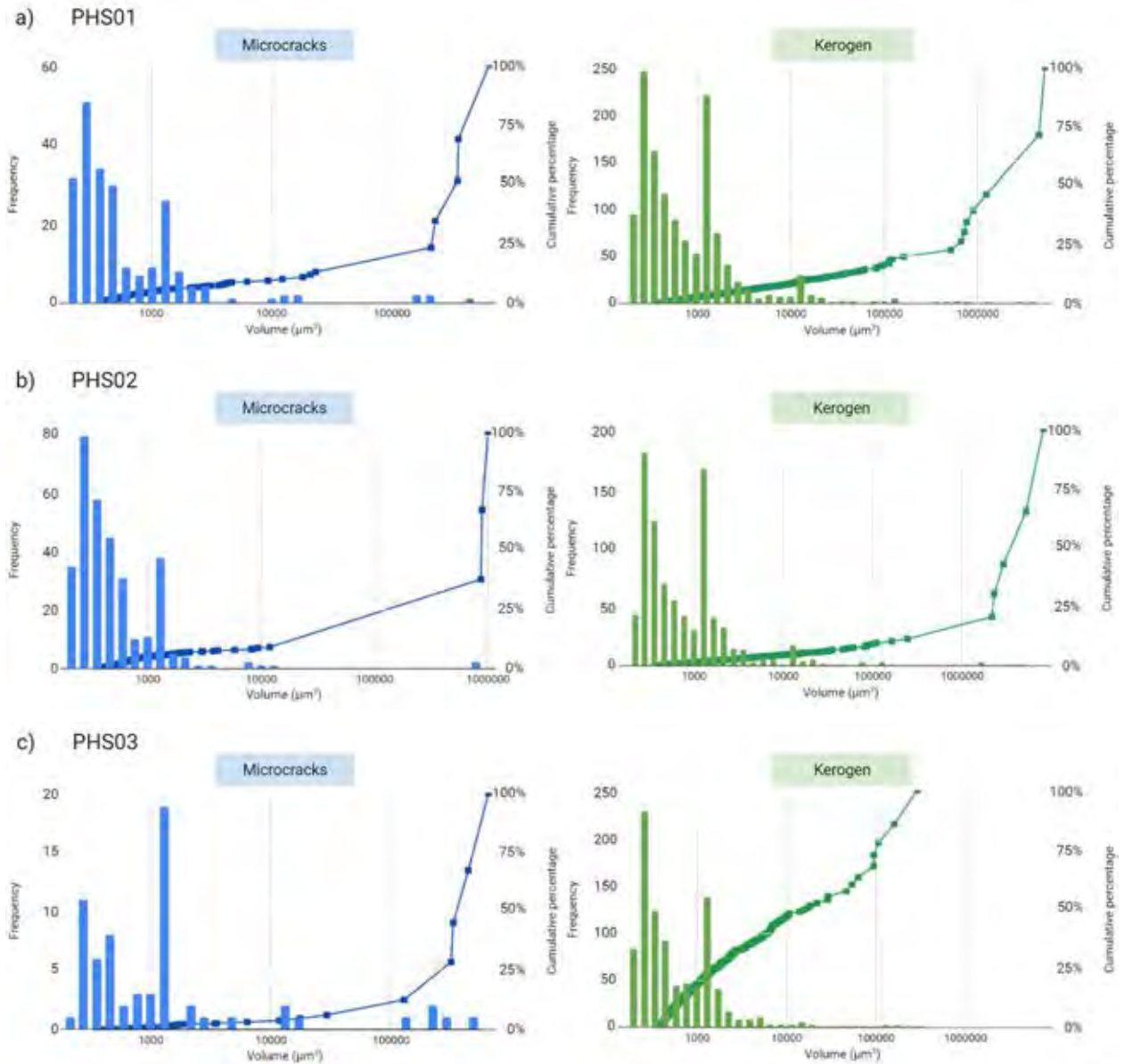
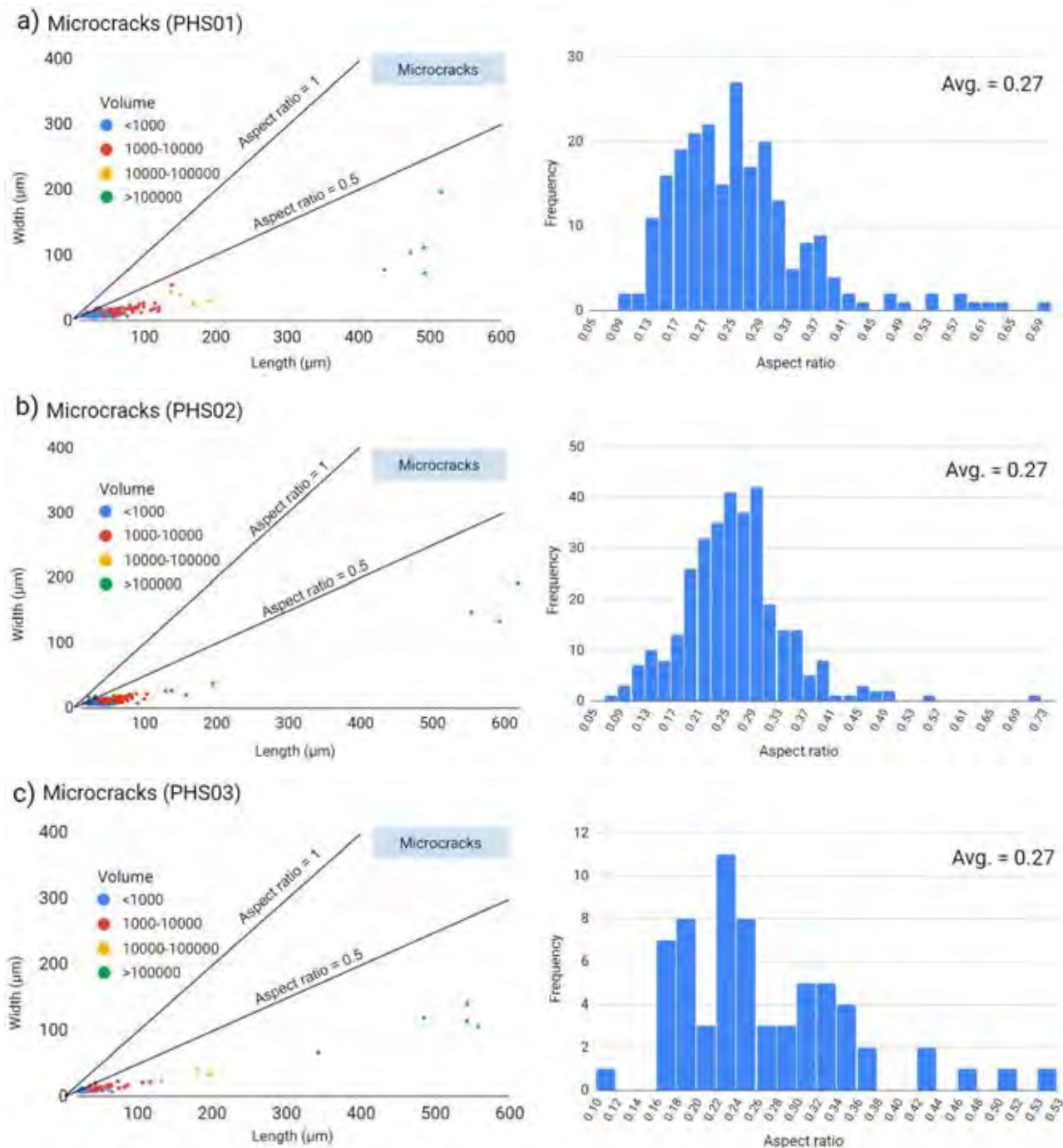


Figure 4.9 Histograms and cumulative percentage of microcracks (left) and kerogen (right) in samples a) PHS01, b) PHS02, and c) PHS03

4.3 3D geometry and orientation

The aspect ratio shows the geometry of microcracks and kerogen in our samples. Materials, which have an aspect ratio (width: length) close to 1 are considered to be spherical while those are close to 0 are considered to be elongated. In Figure 4.10, the graph between width and length shows that the geometry of microcracks and kerogen are mostly elongated.

The average aspect ratios of microcracks and kerogen from all samples are 0.27 and 0.34, respectively. Elongated-geometry materials could present their orientation.



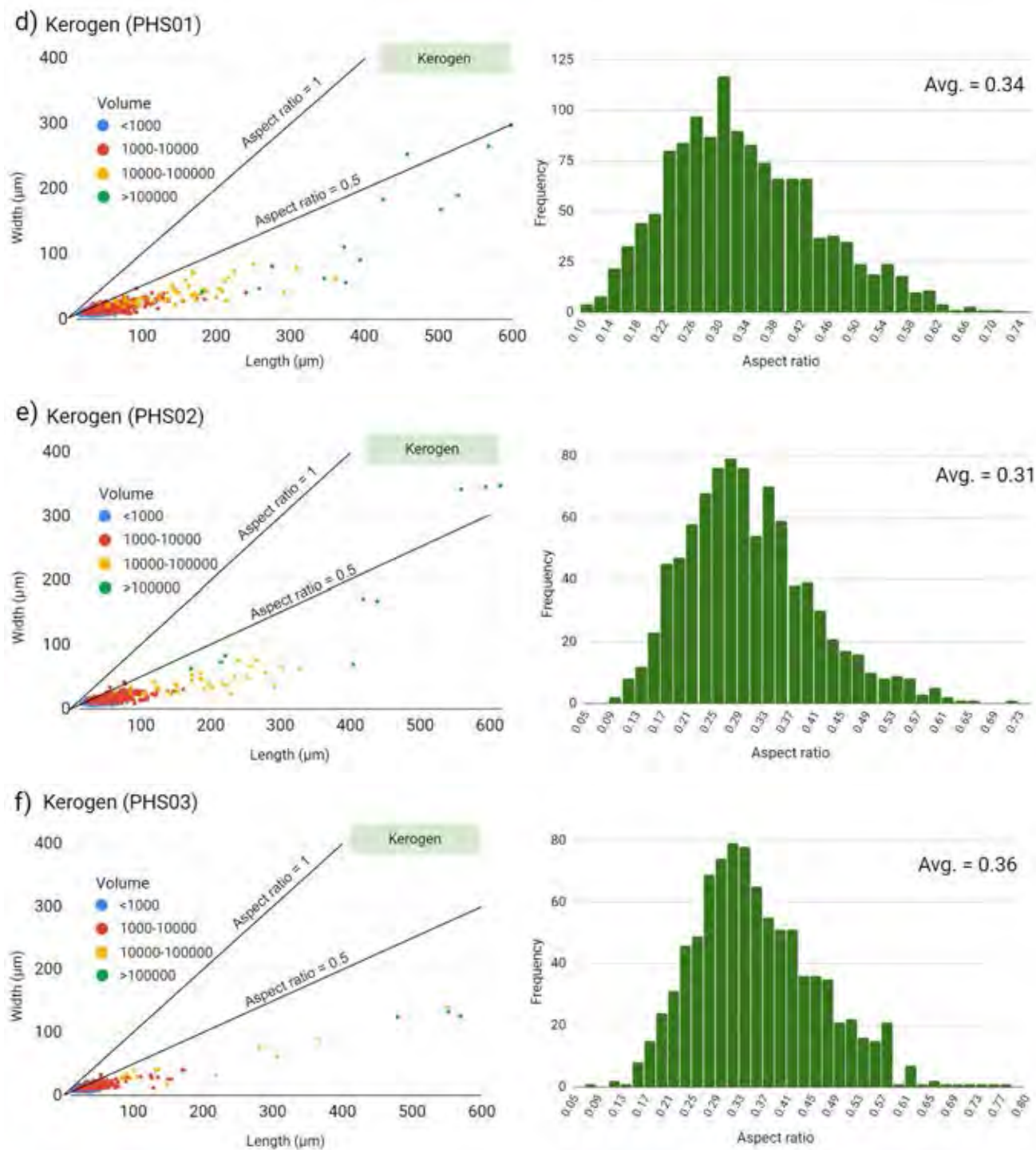


Figure 4.10 Width-length plot and aspect ratio histogram of microcracks (a,b,c) and kerogen (d,e,f)

In the next step, the distribution of microcracks and kerogen will be determined by using the Rose diagram. These elongated materials have directions that are oriented obviously on the XY plane (Figure 4.11).

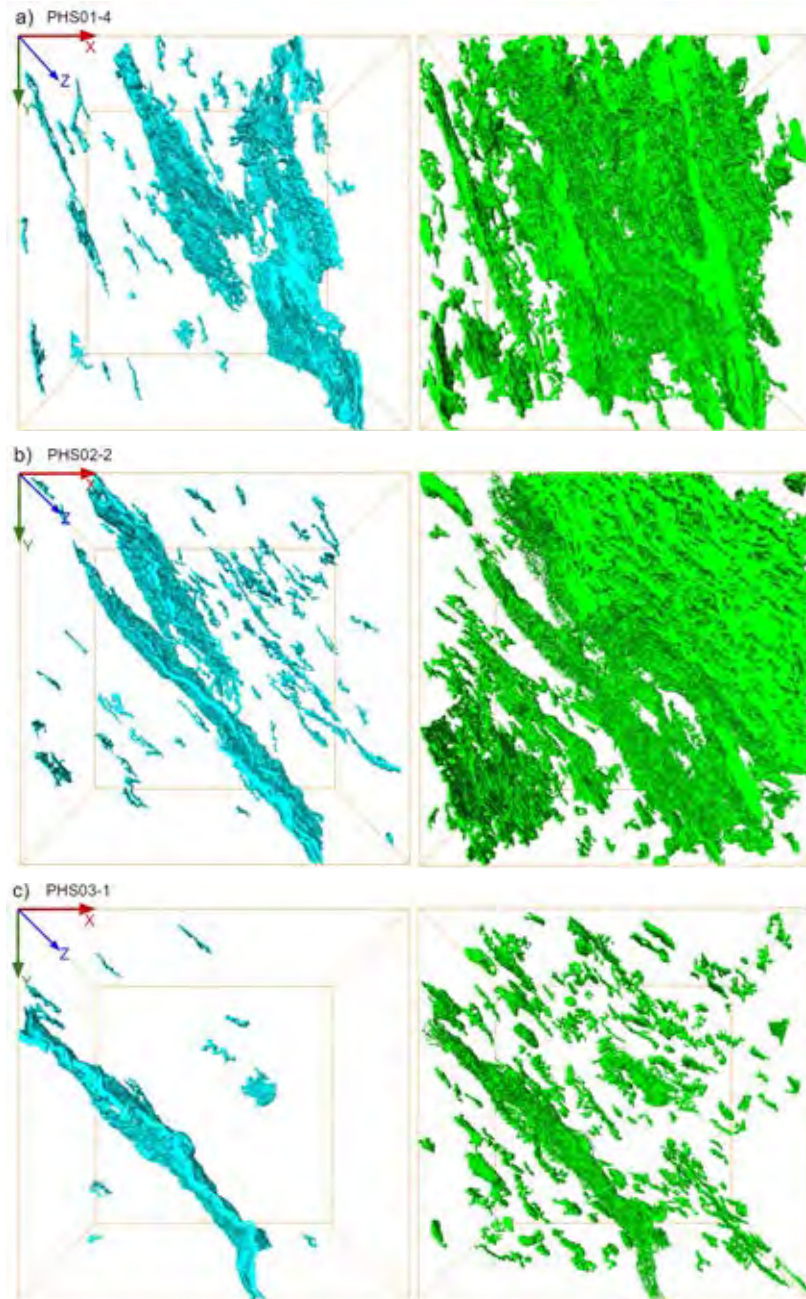


Figure 4.11 Views on XY plane of 3D segmentation show the orientation of microcrack and kerogen in the sample a) PHS01-4, b) PHS02-2, and c) PHS03-1

The rose diagrams in Figure 4.12 show the main direction of microcracks and kerogen of samples. The main direction of microcracks and kerogen (median of data set) of PHS01 are oriented at 105.9° and 105.6° . The PHS02 are oriented at 130.5° and 123.5° while the PHS03 are oriented at 130.9° and 134.6° , respectively.

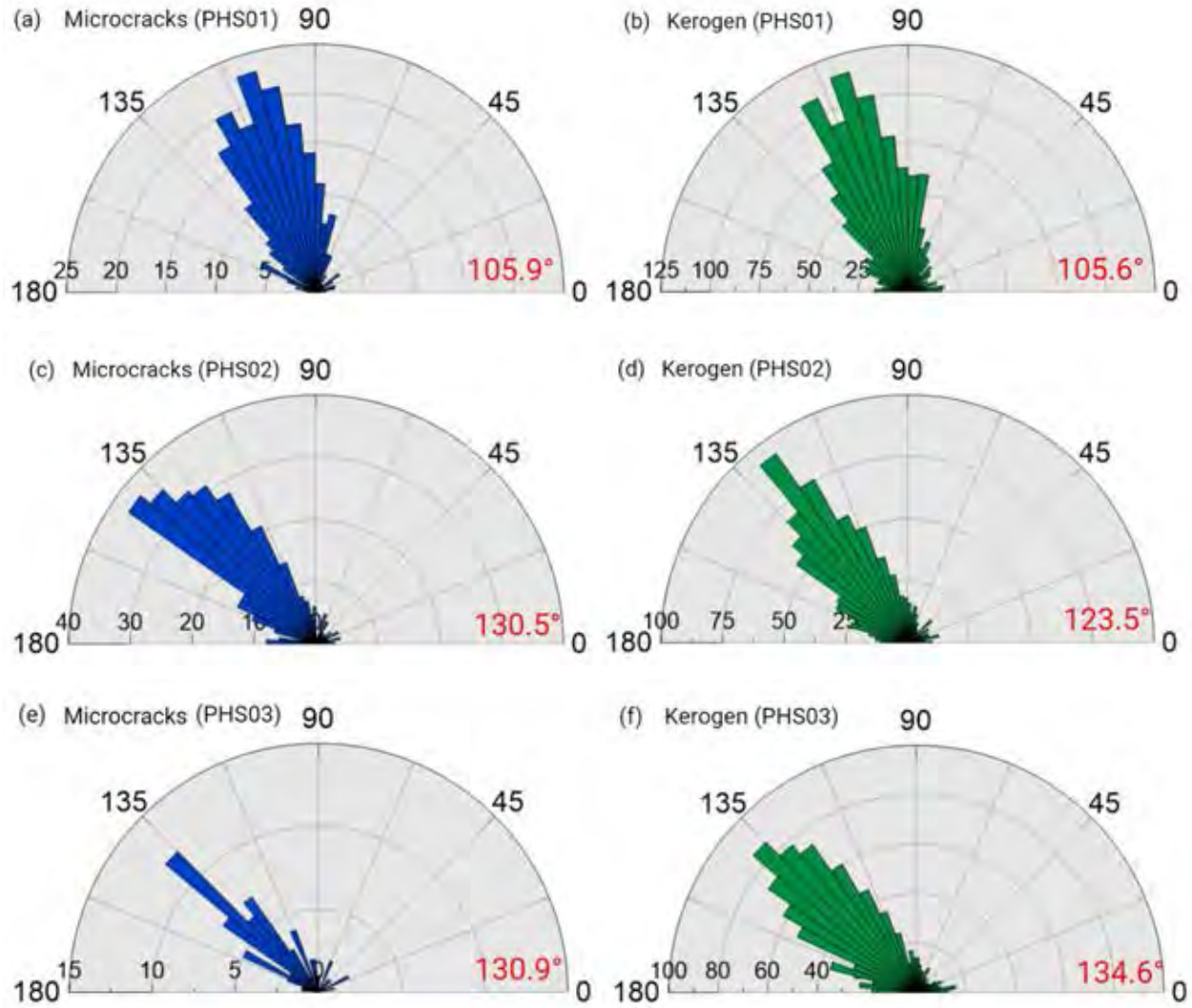


Figure 4.12 Rose diagrams of (a) microcracks, (b) kerogen from PHS01, (c) microcracks, (d) kerogen from PHS02, (e) microcracks, (f) kerogen from PHS03

CHAPTER V

DISCUSSIONS AND CONCLUSION

5.1 Discussions

5.1.1 2D observations

Various pore types were found under micro-scale resolution 2D images. A few interparticle pores such as pores between grains and pores at the edge of rigid grains and intraparticle pores such as intercrystalline pores within pyrite framboids and pores within fossil bodies were presented with a small number comparing to overall pore volume. Previous study using scanning electron microscope (SEM), nano-scale imaging tool, have presented other types of pore which are absent in our samples such as intraplatelet pores within clay aggregates in and dissolution-rim pores in the Ursa Basin shale and Pine Island shale (Loucks et al., 2012). Interparticle and intraparticle pores typically exist in shale samples but very small and nano-scale observation is necessary for imaging these small features in our samples. Organic-matter pores were rarely found in our samples and do not have a significant effect on total pore volume. A study of the Longmaxi shale on multiscale characterization by Wang et al. (2019) suggests that the size of the organic-matter pore is ranging in scale down to nano-scale cause inaccurate observation for this pore type in our research. However, notable fracture pores or microcracks play an important role in our shale samples due to large quantities and pore volume. Certain microcracks were specifically identified into kerogen-edge cracks and perpendicular cracks as observed in artificial maturation experiment in Kimmeridge shale sample by Allan et al. (2014) supports that they are a result of organic-matter maturation. Organic-matter pores, kerogen-edge cracks, and perpendicular cracks often coexist.

5.1.2 Volume fractions and size distributions

Volume fractions of pore and kerogen were calculated (Table 5.1). Porosities of the Phitsanulok shales, shale samples in this research, are 1.47%, 1.98%, and 1.12% for PHS01, PHS02, and PHS03 respectively. Most of the pore volumes in these three shale samples are from large pores, especially, microcracks. A previous study of shale with X-ray micro-computed tomography technique by Mehrabi et al. (2017) shows that different porosities are ranging from 0.29% - 0.96%. The porosities of studies analyzed with X-ray micro-computed tomography are comparable though the phitsanulok shales have a bit higher porosity due to denser existence of

microcracks. Conversely, Gacheta and Middle East shale, studies by Ceron et al. (2013) and Almarzooq et al. (2014) have been analyzed with 3D FIB-SEM technique in nano-scale. Porosities obtained by this FIB-SEM technique are generally higher (5.1% and 2.5% for Gacheta and Middle East shale respectively). The reasonable reason for different porosity is that the 3D FIB-SEM technique accounts for nano-scale pores such as interparticle, intraparticle, and organic-matter pore. Kerogen volume fractions of shale samples are 10.60%, 12.97%, and 1.93% for PHS01, PHS02, and PHS03. While kerogen value in Gacheta and Middle East shale are 4.7% and 9.3% by volume respectively. These kerogen volume fractions can be concluded that shales are very heterogeneous in kerogen content and difficult to differentiate.

Table 5.1 Comparison of porosity, kerogen, and permeability in shale from other studies

Sample	Method	Porosity (%)	Kerogen (v/v%)	Permeability (md)
PHS01	Micro-CT	1.47	10.60	14.60
PHS02	Micro-CT	1.98	12.97	20.04
PHS03	Micro-CT	1.12	1.93	18.18
Unnamed shale (Mehrabi et al., 2017)	Micro-CT	0.29 - 0.96	3.93 - 12.56*	$(5.5 - 92.3) \times 10^{-6}$
Gacheta shale (Ceron et al., 2013)	3D FIB-SEM	5.1	4.7	9.28×10^{-4}
Middle East shale (Almarzooq et al., 2014)	3D FIB-SEM	2.2 - 3.2	9.3 - 18.5	$(1.9 - 5.0) \times 10^{-5}$

*Converted from w.t% using a mean density of 1.65 g/cm^3

5.1.3 3D geometry and orientation

The aspect ratio of pores and kerogen were obtained from all samples. The aspect ratios of pores are 0.27 for PHS01, PHS02, and PHS03. In comparison to a study by Mehrabi (2017), the aspect ratios are in the range of 0.42 - 0.56 which is higher than our samples. The aspect ratio shows that pores from the Phitsanulok shales have more crack-like geometry as they were dominated by microcracks. While pores in shales studied by Mehrabi (2017) are more spherical. The difference of pore aspect ratios indicates different types of pores dominating in shale samples. The aspect ratios of kerogen (0.34, 0.31, and 0.36 for PHS01, PHS02, and PHS03) indicate that they mostly have patch-shape geometry. The aspect ratio of kerogen is not extensively studied and difficult to compare. However, these microcracks and kerogen patches oriented in the explicit direction which parallels to bedding plane. The inclination between microcracks and kerogen patches in each sample is small (less than 7°).

5.1.4 Permeability

Digital flow simulations were generated in three axes (X, Y, and Z) to obtain permeabilities of three VOIs and observe how the orientation of microcracks affect to the direction of fluid flow. Generally, permeabilities are higher than those previous studies (Table 5.1) due to a large connected pore type. Microcracks allow fluid flow easier than those isolated pore. Besides, permeabilities are greater in Z-axis which is the main direction of bedding plane and microcracks (Table 5.2). However, these permeabilities cannot be used to represent the formation because shales are naturally heterogeneous and only VOIs that have microcracks are chosen for this experiment.

Table 5.2 Comparison of permeabilities in X, Y, and Z axes

Sample - VOI	Permeability (md)		
	X	Y	Z
PHS01-1	11.98	13.87	14.60
PHS02-2	10.68	11.73	20.04
PHS03-1	15.29	10.07	18.18

5.2 Conclusion

The results from Syn-MCT suggest that various pore types such as pores between grains, pores at the edge of rigid grains, intercrystalline pores within pyrite framboids, pores within fossil bodies, organic-matter pores, and fracture pores (microcracks) were found in shale samples. Organic-matter pores often coexist with perpendicular cracks and kerogen edge cracks. Porosities in the Phitsanulok shale samples are ranging from 1.12-1.98% mainly calculated from microcracks. Other minor pore types such as interparticle pore and intraparticle pore were found and accounted for very small volume. Kerogen values have a wide range of 1.93-12.97% by volume. Major pores in samples have crack-like geometry (average aspect ratio = 0.27), while kerogen has patch-like geometry (average aspect ratio = 0.34). Microcracks and kerogen have obvious orientation parallel to the bedding plane. Moreover, these cracks significantly influence fluid transport properties of shale.

References

- Ainsworth, R.B., Sanlung, M., and Duivenvoorden, S.T.C. 1999. Correlation Techniques, Perforation Strategies, and Recovery Factors: An Integrated 3-D Reservoir Modeling Study, Sirikit Field, Thailand. AAPG Bulletin 83 (1999).
- Allan, Adam M., Vanorio T., and Jeremy E. P. D. 2014. Pyrolysis-induced P-wave Velocity Anisotropy in Organic-rich Shales. *Geophysics* 79, no. 2 (03, 2014).
- Almarzooq, A., AlGhamdi, T., Koronfol, S., Dernaika, M., & Walls, J. 2014. Shale Gas Characterization and Property Determination by Digital Rock Physics. Society of Petroleum Engineers.
- Bal, A.A., Burgisser, H.M. Harris, D.K., Herber, M.A., Rigby, S.M., Thumprasertwong, S., and Winkler, F.J. 1992. The Tertiary Phitsanulok lacustrine basin, onshore Thailand. Proceedings of the National Conference on Geologic Resources of Thailand: Potential for Future Development, Department of Mineral Resources: Bangkok, Thailand, 1992, p. 247-258.
- Boonyasatphan, P. 2017. Reservoir Characterization for Unconventional Resource Potential, Pitsanulok Basin, Onshore Thailand. Dissertations And Theses; Thesis (M.S.)--Colorado School of Mines, 2017.; Publication Number: AAT 10269594; ISBN: 9780355055511; Source: Masters Abstracts International, Volume: 56-05.; 122 p.
- Ceron M., Walls J.D., and Diaz, E. 2013. Comparison of Reservoir Quality from La Luna, Gacheta and Eagle Ford Shale Formations Using Digital Rock Physics. AAPG International Conference and Exhibition, Cartagena, Colombia, September 8-11, 2013.
- C&C Reservoir. 2009. Field Evaluation Report, Far East, Sirikit Field, Phitsanulok Basin, Thailand. Field Analogs report (2009).
- Department of Mineral Resources. 2014. Geology of Thailand: Department of Mineral Resources, Ministry of Natural Resources and Environment, Bangkok, Thailand. 508 p. II
- Flint, S., Stewart D.J., and Van Riessen E.D. 1989. Reservoir geology of the Sirikit oilfield, Thailand: lacustrine deltaic sedimentation in a Tertiary intermontane basin. Geological Society, London, Special Publications 41, no. 1 (1989): 223-35.

- Flint, S., Stewart, D.J., Hyde, T., Gevers, E.C.A., Dubrule, O.R.F., and van Riessen, E.D. 1988. Aspects of reservoir geology and production behavior of Sirikit oil field, Thailand—An integrated approach. *American Association of Petroleum Geologists Bulletin*, v. 72, no. 7, p. 1254–1269.
- Galkin, S., Efimov, A., Krivoshchekov, S., Savitskiy, Y., and Cherepanov, S. 2015. X-ray tomography in petrophysical studies of core samples from oil and gas fields. *Russian Geology and Geophysics*, 56(5), 782-792.
- Jacobs, P., & Cnudde, V. 2009. Applications of X-ray computed tomography in engineering geology' or 'looking inside rocks ...'. *Engineering Geology*, 103(3-4), 67-68.
- Kanitpanyacharoen, W., Parkinson, D. Y., Carlo, F. D., Marone, F., Stampanoni, M., Mokso, R., MacDowell, A., and Wenk, H. 2013. A comparative study of X-ray tomographic microscopy on shales at different synchrotron facilities: ALS, APS and SLS. *Journal of Synchrotron Radiation*, 20(1), 172-180.
- Ketcham, R. A., and Carlson, W. D. 2001. Acquisition, optimization and interpretation of X-ray computed tomographic imagery: Applications to the geosciences. *Computers & Geosciences*, 27(4), 381-400.
- Knox, G. and Wakefield, L. 1983. An Introduction to the Geology of the Phitsanulok Basin. Conference on geology and resource of Thailand, Bangkok.
- Kobchenko, M., Panahi H., Renard F., Dysthe D.K., Malthe-Sørensen A., Mazzini A., Scheibert J., Jamtveit B., and Meakin P. 2011. 4D Imaging of Fracturing in Organic-rich Shales during Heating. *Journal of Geophysical Research* 116, no. B12 (12, 2011).
- Lawwongngam, K., and Philp, R.P. 1991. Geochemical characteristics of oils from the Sirikit Oilfield, Phisanulok Basin, Thailand. *Chemical Geology*, v. 93, p. 129-146.
- Lawwongngam, K., and Philp, R.P. 1993. Preliminary investigation of oil and source rock organic geochemistry from selected Tertiary basins of Thailand: *Journal of South Asian Earth Sciences*, v. 8, nos. 1–4, p. 433–448.

- Loucks, R.G., Reed, R., Ruppel, S., and Hammes U. 2012. Spectrum of Pore Types and Networks in Mudrocks and a Descriptive Classification for Matrix-related Mudrock Pores. AAPG Bulletin 96, no. 6 (06, 2012): 1071-098.
- Mehrabi, M., Pasha M., Hassanpour A., Glover P., and Jia, X. 2017. Imaging and Quantification of the Pore Microstructure of Gas Shales Using X-ray Microtomography. Solid Earth Discussions, 06, 2017, 1-17.
- Morley, C.K., Woganan, N., Sankumarn, N., Hoon, T.B., Alief, A., and Simmons, M. 2001. Late Oligocene–Recent stress evolution in rift basins of northern and central Thailand—Implications for escape tectonics. Tectonophysics, v. 334, p. 115–150.
- Morley, C.K. 2009. Evolution from an oblique subduction back-arc mobile belt to a highly oblique collisional margin: The Cenozoic tectonic development of Thailand and eastern Myanmar. in Cawood, P.A., and Kroner, A., eds., Earth Accretionary Systems in Space and Time: Geological Society, London, Special Publications 2009 No. 318, p. 373–403.
- Morley, C.K., and Racey, A. 2011. Tertiary stratigraphy. The Geology of Thailand, 223-271.
- Panahi et al. 2012. A 4D Synchrotron X-Ray-Tomography Study of the Formation of Hydrocarbon- Migration Pathways in Heated Organic-Rich Shale. SPE Journal, vol. 18, no. 02, 2012, pp. 366–377.
- Pinyo and Komon. 2011. Unconventional petroleum system evaluation of the Chum Saeng Formation, Phitsanulok Basin, Thailand in International Conference on Geology. Geotechnology, and Mineral Resources of Indochina [GEOINDO]: 11th Conference Proceedings, Khon Kaen University, Department of Geotechnology, Khon Kaen, Thailand, December 1–3, 2011, p. 267–280.
- Polachan, S., Pradidtan S., Tongtaow C., Janmaha S., Intarawijitr K., and Sangsuwan C. 1991. Development of Cenozoic Basins in Thailand. Marine and Petroleum Geology 8, no. 1 (02 1991): 84-97.

- Rodriguez, R., Crandall, D., Song, X., Verba, C., and Soeder, D. 2014. Imaging Techniques for Analyzing Shale Pores and Minerals. NETL-TRS-6-2014; NETL Technical Report Series; U.S. Department of Energy, National Energy Technology Laboratory: Morgantown, WV, 2014; p 40.
- Smit, J.. 1999. Oil recovery and fracture distribution in Basement reservoirs. European Association of Geoscientists and Engineers 61st conference and Technical Exhibition, Helsinki, Paper 5-07, 4 p.
- Thamniyom P. 2012. Depositional Environment of Basal Pratu Tao Formation in Thap Raet Phitsanulok Basin. Thailand Bulletin of Earth Sciences of Thailand (BEST) : (Vol.5 No.2, October 2012) : 102 - 107.
- USGS 2014, Schenk, Christopher J., Ronald R. Charpentier, Timothy R. Klett, Tracey J. Mercier, Marilyn E. Tennyson, Janet K. Pitman, and Michael E. Brownfield. 2014. Assessment of Potential Unconventional Lacustrine Shale-oil and Shale-gas Resources, Phitsanulok Basin, Thailand. Fact Sheet, 2014.
- USGS Phitsanulok Basin Assessment Team. 2014. Geology and assessment of unconventional resources of Phitsanulok Basin, Thailand. U.S. Geological Survey Open-File Report 2014-1133, 1 sheet.
- Wang, Y., Carlo, F.D., Mancini, C., McNulty, I., Tieman, B., Bresnahan, J., Foster, I., Insley, J., Lane, P., von Laszewski, G., Kesselman, C., Su, M.-H. and Thieboux, M. 2001. Rev. Sci. Instrum. 72, 2062-2068.
- Wang Y., Wang L., Wang J., Jiang Z., Wang C., Fu Y., Song Y., Wang Y., Liu D., and Jin C. 2019. Multiscale characterization of three-dimensional pore structures in a shale gas reservoir: A case study of the Longmaxi shale in Sichuan basin, China. Journal of Natural Gas Science and Engineering, Volume 66, 2019, Pages 207-216,

